UNIVERSITY OF CALIFORNIA SAN DIEGO

On-Chip Integrated Nano-Scale Light Sources and Switches for Optical Interconnect

A dissertation submitted in partial satisfaction of the

requirements for the degree Doctor of Philosophy

in

Materials Science and Engineering

by

Cheng-Yi Fang

Committee in charge:

Professor Yeshaiahu Fainman, Chair
Professor Zhaowei Liu
Professor Yu-Hwa Lo
Professor Ivan Schuller
Professor Paul Yu

2019

The Dissertation of Cheng-Yi Fang is approved, and is acceptable in quality and form for publication on microfilm and electronically:

_____

_____

_____

_____

_____

Chair

University of California San Diego

2019

Table of Contents

List of Figures

List of Tables

Acknowledgements

I would like to thank Professor Shaya Fainman for providing the opportunity to do research. The lab cultural is well established and we can explore what we are interested with full support and no distraction.

I would like to thank Dr. Felipe Vallini and Dr. Abdelkrim El Amili for the mentorship and guidance in the past few years with patience. I also want to thank Dr. Hung-Hsi Lin and Dr. Mu-Han Yang for a lot of help and useful suggestion. I would like to thank my fellow graduate students for the fruitful discussion.

I would like to thank nano3 staff members for the help in fabrications.

I would like to thank all my friends and those who are still working on their way to graduation. The hardship of pursuing a PhD can only be understood when you really devoted yourself to it.

I also want to thank my family and Wan-Tzu for all the supports. I am thankful for your understanding to spend six year for the degree. You are the one who make this journey possible.

Chapter 2, in part, is a reprint of the material as it appears "Low resistance tunnel junctions for efficient electrically pumped nanolasers. " Fang, C. Y., Vallini, F., El Amili, A., Smalley, J. S., & Fainman, Y. (2017). *IEEE Journal of Selected Topics in Quantum Electronics*, 23(6), 1-6. The dissertation author was the primary coinvestigator and coauthor of this paper.

Chapter 3, in part, is a reprint of the material as it appears "Lasing Action in Low Resistance Nanolasers based on Tunnel Junctions." Fang, Cheng-Yi, Si Hui Pan, Felipe Vallini, Antti Tukiainen, Jari Lyytikäinen, Gustav Nylund, Boubacar Kanté, Mircea Guina, Abdelkrim El Amili, and Yeshaiahu Fainman *(in submission)*. The dissertation author was the primary coinvestigator and coauthor of this paper.

Chapter 4, in part, is a reprint of the material as it appears "Microwave signal switching on a silicon photonic chip." Fang, Cheng-Yi, Hung-Hsi Lin, Mehdi Alouini, Yeshaiahu Fainman and Abdelkrim El Amili. *(in submission)* The dissertation author was the primary coinvestigator and coauthor of this paper.

Vita

2010 Bachelor of Science, National Taiwan University, Taiwan.

2012 Master of Science, National Taiwan University, Taiwan

2019 Doctor of Philosophy, University of California San Diego, La Jolla.

PUBLICATIONS

Journal Article

- **Fang, Cheng-Yi**, Felipe Vallini, Abdelkrim El Amili, Joseph ST Smalley, and Yeshaiahu Fainman. "Low resistance tunnel junctions for efficient electrically pumped nanolasers." *IEEE Journal of Selected Topics in Quantum Electronics* 23, no. 6 (2017): 1-6.
- **Fang, Cheng-Yi**, Hung-Hsi Lin, Mehdi Alouini, Yeshaiahu Fainman, and Abdelkrim El Amili. "Reconfigurable On-chip Photoconductive Switches." *arXiv preprint* arXiv:1905.05228 (2019).
- Chen, Zijun, Suruj S. Deka, Si Hui Pan, Sizhu Jiang, **Cheng-Yi Fang**, Yeshaiahu Fainman, and Abdelkrim El Amili. "Intensity noise and bandwidth analysis of nanolasers via optical injection." *Optics Express* 27, no. 6 (2019): 8186-8194.

Conference Paper

- **Fang, Cheng-Yi**, Felipe Vallini, Abdelkrim El Amili, Antti Tukiainen, Jari Lyytikäinen, Mircea Guina, and Yeshaiahu Fainman. "Development of Efficient Electrically Pumped Nanolasers based on InAlGaAs Tunnel Junction." *In 2018 Conference on Lasers and Electro-Optics (CLEO)*, pp. 1-2. IEEE, 2018.

- Hong, Brandon, Felipe Vallini, **Cheng-Yi Fang**, Amr Alassad, and Yeshaiahu Fainman. "Low-cost thermal infrared detector based on surface plasmon resonance imaging." *In CLEO: QELS_Fundamental Science*, pp. JW2A-73. Optical Society of America, 2017.

ABSTRACT OF THE DISSERTATION

On-Chip Integrated Nano-Scale Light Sources and Switches for Optical Interconnect

by

Cheng-Yi Fang

Doctor of Philosophy in Materials Science and Engineering

University of California San Diego, 2019

Professor Yeshaiahu Fainman, Chair

The rapidly growing global internet traffic requires ever faster data transfer within computer networks. Photonic integrated circuits can pave the way to accelerated signal transmission and increase bandwidth of optical interconnects in a compact way. One of the key building blocks for photonic integrated circuits is an on-chip nanolaser. In this dissertation, we explore ways to reduce resistance and the Joule heating of the nanolasers We experimentally

demonstrated an electrically pumped nanolaser by incorporating a tunnel junction. The resistance is reduced, so as the threshold voltage and joule heating. Besides nanolasers, an optically controlled microwave switch is another essential component in photonic integrated circuits. We designed and demonstrated a Monolithic Optically Reconfigurable Integrated Microwave Switches (MORIMSs) as a more efficient and integrated photoconductive switch. The two devices we explore in this dissertation have the potential to be essential building blocks for photonic integrated circuits in the future.

Chapter 1. Introduction

Based on the report from Cisco Systems, annual global IP traffic would reach over zettabyte in 2016 and will reach 2.3ZB by 2020. It estimated global IP traffic will grow at a compound annual growth rate of 22% from 2015 to 2020 [1]. Although electronic circuit and copper wires have been proved to be efficient and reliable to handle the global data traffic in the past, they suffered from RC delay which is the bottleneck to scaling and interaction with one another and the copper wire which means they cannot meet the demand of such fast growing data transfer in the future.

Photonics technology using photons instead of electrons for carrier generation, detection, and manipulation through emission, transmission, modulation, signal processing, switching, amplification, and sensing, has become a good candidate to accelerate signal manipulation and boost bandwidth capacity. Compared to electron, photons move at the speed of light and has no interference issue. Therefore, photons can transmit great amounts of information without the same restriction electronic circuits has. Since the invention of laser and optical fiber, photon handle essentially all of the long distance telecommunications and have dramatic increased the capacity. For information processing and data transmission within shorter distance down to the electronic chips or interconnection, they are still challenges to be conquered.

The development of photonics started from ‘60s at Bell Labs [2]. Nowadays, the integrated photonics or photonics integrated circuits, PICs are quite different from the prototype at that time. With the demand of the market and the improvement of the material technology in silicon, silica and III-V compounds, photonic has become a promising technology for numerous applications including data centers, 5G communications and augmented reality. Integrated optics make a

stronger contender for high speed networks because of their potential for higher bandwidth, lower latency, lower energy consumption, and scalability[3], [4] .

Photonics integrated circuits are mostly built on Silicon thanks to the mature C-MOS (Complementary metal–oxide–semiconductor) industry. Optical waveguides, similar to optical fibers, guide light in high index and transparent core materials (Si) surrounded by low index cladding materials. with different cross sections such as rib, ridge or slot structure have different guiding core surrounded by low index cladding materials [2]. Silicon on insulator (SOI) wafer, which there is a buried oxide layer under the Si device layer are widely used in PICs. Si as the device layer is transparent at telecommunication wavelength and the low index SiO_2 layer provide index contrast for optical mode confinement.

Si is a perfect material for most of the PIC component including waveguides, modulators, mode converters, couplers and splitter etc. However, it is indirect bandgap, which means it is not suitable for light source. III-V materials such as GaAs, InP or InGaAs must be used for photon generation. Therefore, developing on-chip light source is essential. In this dissertation we explore new design and fabrication approaches III-V nanolasers.

Besides the active light source, microwave photonics is another essential field to be explored which uses light to carry and process microwave signals over a photonic link. Light can instead be used as a stimulus to microwave devices that directly control microwave signals. Such optically controlled amplitude and phase-shift switches are investigated for use in reconfigurable microwave systems, but they suffer from large footprint, high optical power level required for switching, lack of scalability and complex integration requirements, restricting their implementation in practical microwave systems. Therefore, to develop monolithic optically reconfigurable microwave switches integrated in CMOS compatible silicon photonic chip is necessary. In

this dissertation, we report Monolithic Optically Reconfigurable Integrated Microwave Switches (MORIMSs) built on a CMOS compatible silicon photonic chip that addresses all of the stringent requirements. In this chapter we give a brief overview of state of the art nanolaser and photoconductive switches.

Chapter 2 describes the theoretical analysis on the effect of adding an InGaAsP tunnel junction for efficient carrier injection in metallo-dielectric nanolasers. With our theoretical model we show that the device resistance is reduced by a factor of ~6.5. The applied voltage at the room temperature lasing threshold is reduced from 3.05V to 1.35V, a reduction of 69% in heat generation, whereas the Q-factor and gain threshold of the cavity are not degraded.

Chapter 3 demonstrates experimentally lasing action of a new nanolaser design with a tunnel junction. By using a heavily doped tunnel junction for hole injection, we can replace the p-type contact material of a conventional nanolaser diode with a low-resistance n-type contact layer. This leads to a significant reduction of the device resistance and lowers the threshold voltage from 5 V to around 0.95 V at 77 K. Because of less Joule heating during current injection, the nanolaser can be operated at temperatures as high as 180 K under CW pumping.

Chapter 4 reports Monolithic Optically Reconfigurable Integrated Microwave Switches (MORIMSs) built on a CMOS compatible silicon photonic chip that addresses the stringent requirements. Our scalable micrometer-scale switches provide higher switching efficiency and require optical power orders of magnitude lower than the state-of-the-art. Also, it opens a new research direction on silicon photonic platforms integrating microwave circuitry.

Chapter 5 Concludes the contributions of this dissertation and discusses possible future research directions.

1.1. The development of Nanolasers

Photonic devices have the potential to replace the electronic devices and circuits in the future which bandwidth is inherently limited by resistor-capacitor (RC) time delays. Similar to Moore's Law in electronic devices, reducing the foot print of photonics devices leads to a higher packing density and lower power consumption. Among various optical devices, laser, the light source in optical interconnect, is one of the most essential components. Since the first laser was first demonstrated in 1960 [5], the dimension has been reduced from meter to millimeter scale thanks to solid-state laser diodes [6]. Later in 1979, GaInAsP/InP vertical-cavity surface-emitting laser (VCSEL) was invented [7] which reduced the device dimension down to tens of micrometers. Further miniaturization down to nanometer was enabled by Hill and colleagues in late 2000 [8]. They demonstrated the first metal-clad semiconductor nanolaser. Since then nanoscale semiconductor lasers have attracted growing interest because their small footprints may enable densely-packed chip-scale photonic circuits for various applications including optical interconnections, switching, sensing, displays and efficient lighting [9].

Different types of nanolaser have their own characteristics.

VCSELs, which employ high-reflectivity distributed Bragg reflectors (DBRs) – on both sides of the MQW active region has been commercially available since late 1990s [10]. Although DBRs provide high-reflectivity which guarantee high quality factor (Q) cavities. The thickness of the devices are unavoidably on the order of tens of micrometer.

Photonic Crystal Defect Cavity Lasers is another branch of nanolasers. All these lasers consist of sub-wavelength periodic structure called photonic crystal. Each photonic crystal has its own photonic band gap in which light with wavelength falling in the band gap cannot exist. Therefore, a defect in the photonic crystal can confine light to diffraction-limited volumes leading

to a high-Q cavity. The first theoretical demonstration of photonic crystal defect cavity lasers was in 1999 [11]. In the same year the first device was also demonstrated by Painter et al. [12] However, even though the optical mode is well confined in the nanometer scale, the devices are still very large which is not ideal to reduce the foot print.

Besides DBRs and photonic crystals, using metal is another way to achieve good optical mode confinement. Plasmonic mode nanowire lasers are quasi-1D structures with diameters less than hundreds of nanometers. The unique design proposed by [13] Oulton et al. allows the propagation of SPPs over long distances. In 2012, Lu et al. demonstrated a InGaN/GaN core-shell hexagonal nanowires with a smooth epitaxial silver film growth technique in which all three dimensions are subwavelength [14]. In 2014, Zhang et al. demonstrated an efficient room temperature ultraviolet low-threshold plasmonic nanolaser [15].

Another type of nanolaser utilizing surface plasmon called SPASER (Surface Plasmon Amplification by Stimulated Emission of Radiation) was demonstrated in 2003 by Bergman and Stockman [16]. In this design a V-shaped metallic inclusion plane surrounded by a gain media can support strongly localized plasmon modes which generate temporally coherent light.

For nanowire laser, it not necessary to use metal as the cladding layer. All-dielectric nanowires lasers have a high contrast between the refractive indices of the wires and the surroundings. The first nanowire laser using ZnO nanowires showed lasing peal in ultraviolet (UV) regime [17] Since then, different active materials showing lasing peak at different wavelength spanning from UV to near IR have been demonstrated, including GaN [18], [19], CdS [20], CdSe [21] , CdSSe [22], GaAs [23], InGaAs [24], AlGaAs [25], ZnS [26], GaSb [27]and InP [28].

However, an essential requirement for many applications of nanolasers is electrical pumping at room temperature. All these types of nanolasers mention above have their own

limitations. Therefore, among the various nanolaser designs, metallo-dielectric nanolasers are excellent candidates for optical sources in chip-scale integrated circuits. Metallo-dielectric nanolasers are based on the metal-clad nanolaser demonstrated by Hill et al. [8]. In this work, metal was directly deposited onto the semiconductor gain medium. Although the metal cladding can suppress leaky optical modes, the large overlap of the mode with the metal makes Q quite low. The main challenge in sub-wavelength lasers is to meet all the requirements for lasing emission while reducing the physical size of the device in all three dimensions. Indeed, shrinking the size of the resonator gives rise to a spatial spreading of the optical mode beyond its physical boundaries. This obviously induces a dramatic increase of the optical loss and thus increases the lasing threshold. To overcome this issue, one approach is to wrap the active medium with a combination of a dielectric shield and a metal layer [29]. By optimizing the thickness of the low index shield between the metal and semiconductor, the gain threshold of the laser can be substantially reduced. The benefit stems from the tendency of the low-index shield to push the electromagnetic mode towards the high-index inner core and away from the metal walls, reducing the mode metal overlap and hence, the Joule loss. This design was first demonstrated by Nezhad et al. [30]

Metallo-dielectric nanolasers also have the advantages of mitigating optical coupling between adjacent devices [31], smaller footprints than photonic crystal lasers [12], [32] ; lower resistance current injection with respect to nanowire lasers[17] , and lower cavity losses than metallic cavities[33], [34], plasmonic lasers[13] and spasers [35].

Metallo-dielectric nanolasers show great optical properties, but realizing continuous-wave (CW) pumped, and room temperature–operating nanolasers is another challenge. The selection of gain medium is critical to the device performance. Vallini et al. has shown that bulk semiconductor

is a better choice than multiple-quantum-wells (MQWs) as the gain medium for electrically pumped metal-clad nanolasers. [36]

Because of their extreme compactness, nanolasers exhibit a large electrical resistance. Therefore, to reach lasing threshold, injecting current into the active region requires higher applied voltages. The generated Joule heat is detrimental to nanolasers and is one of the main limiting factors for room-temperature operation. Therefore, good thermal management and an efficient current injection scheme is necessary for nanolaser operation. Gu et al. has also proposed using Al_2O_3 instead of SiO_2 as the cladding layer because Al_2O_3 possesses better thermal conductivity. [37]

As for the epilayer design Lee et al. proposed and experimentally demonstrated an InGaAs/InP double heterostructure grown on an InP substrate. [31] The 300 nm thick InGaAs layer is the gain media. Highly doped InGaAsP layers on the bottom and top are the electrical contacts and doped InP layers serve as cladding layers through which the current is injected into the active layer.

Moreover, the choice for cavity geometry is important too, cylindrical nanolasers supporting whispering-gallery mode has been demonstrated with great performance [31], [37]. Another cavity design using rectangular device was demonstrated by Ding et al.. [33] In 2013, Ding also demonstrated a CW electrically pumped operation at room temperature. [38]

1.2. The development of photoconductive switches

Optically reconfigurable microwave switches are promising key elements in emerging 5G wireless communications network and future RADAR systems. However, current optically controlled amplitude and phase-shift switches are far from being applied in the aforementioned

applications because of their lack of scalability and complex integration capability and, they require high optical power level for switching operation.

Optical control microwave circuits and systems continues to draw research interests because of its fast response and compact geometry. A Photoconductive Semiconductor Switch (PCSS) is an optoelectronic device based on the phenomenon of photoconductivity. The benefit of using PCSSs is that metallic biasing lines for commercially available microwave switches including Field Effect Transistor (FET) and PIN diodes are not required and thus they are immune to electromagnetic interferences. PCSSs are made of semiconductor materials on which there are metal contacts connecting to electrical circuits. Upon illumination, electron-hole pairs are generated in semiconductor materials and the conductivity on the semiconductor materials increase allowing the electrical signal to be transmitted. Because of their capability of fast triggering, PCSSs not only serve as the element of power electronics but have the application in microwave and terahertz signal generators [39].

The first Si-based photoconductive switch was demonstrated by Auston et al. [40] in 1975. Since then, different semiconductor materials have been studied based on their application and material properties. For example, wide band gap materials like GaN and SiC [39], [41], [42] using 440nm as the illumination source have the benefit of high critical electric field and good thermal conductivity. III-V compound materials including ErAs:InGaAs [43] and GaNAsSb [44]showing short carrier lifetime have been experimentally demonstrated for telecom wavelength operation. GaAs[45]–[47] that utilizes 800nm as the illumination source has the advantage of high speed switch and large on/off ratio. Meanwhile, Si [48]–[51] with the operation wavelength at 800nm or visible regime is also a good candidate. Moreover, the mature Si manufacture technology

enables more complex and compact device design in order to realize on-chip and reconfigurable application.

Chapter 2. Low Resistance Tunnel Junctions for Efficient Electrically Pumped Nanolasers

2.1. Background

Nanoscale semiconductor lasers have attracted growing interest because their small footprints may enable densely-packed chip-scale photonic circuits for various applications including optical interconnections, switching, sensing, displays and efficient lighting [9]. An essential requirement for many applications of nanolasers is electrical pumping at room temperature.

Among the various nanolaser designs, metallo-dielectric nanolasers are excellent candidates for optical sources in chip-scale integrated circuits because of the mitigation of optical coupling between adjacent devices [31], smaller footprints than photonic crystal lasers [12], [32]; lower resistance current injection with respect to nanowire lasers [17], and lower cavity losses than metallic cavities [33], [34], plasmonic lasers [13] and spasers [35]. The main challenge in sub-wavelength lasers is to meet all the requirements for lasing emission while reducing the physical size of the device in all three dimensions. Indeed, shrinking the size of the resonator gives rise to a spatial spreading of the optical mode beyond its physical boundaries. This obviously induces a dramatic increase of the optical loss and thus increases the lasing threshold. To overcome this issue, one approach is to wrap the active medium with a combination of a dielectric shield and a metal layer [29]. By optimizing the thickness of the low index shield between the metal and

semiconductor, the gain threshold of the laser can be substantially reduced. The benefit stems from the tendency of the low-index shield to push the electromagnetic mode towards the high-index inner core and away from the metal walls, reducing the mode metal overlap and hence, the Joule loss.

Because of their extreme compactness, nanolasers exhibit a large electrical resistance. Therefore, to reach lasing threshold, injecting current into the active region requires higher applied voltages. The generated Joule heat is detrimental to nanolasers and is one of the main limiting factors for room-temperature operation. Therefore, good thermal management and an efficient current injection scheme is necessary for nanolaser operation.

The best way to improve the current injection efficiency is to incorporate tunnel junctions into nanolasers as done in light emitting devices with much larger dimensions. For example, vertical cavity surface-emitting lasers (VCSELs) have suffered from poor current injection and spreading [52], [53], while light-emitting diodes (LEDs) have shown lower quantum efficiency and higher operation voltage than the theoretically predicted values [54]. These problems result from the small mobility of holes compared to electrons, which leads to p-contacts with high resistance. This issue is circumvented by replacing the p-type layers with more conductive layers. Therefore, tunnel junctions, formed by a heavily doped PN junction that allows electrons and holes to tunnel through the depletion region under negligible reversed bias, were introduced to replace the p-contact and improve the performance of VCSELs [52], [53], [55], LEDs [54], [56], [57] and, more recently, SOI-Integrated InP-based micro lasers [58], [59, p.]. By incorporating tunnel junctions, both contacts are n-type materials which significantly alleviates current injection problems.

In this chapter, we demonstrate how the incorporation of a tunnel junction into our metallo-dielectric nanolaser design improves its electrical performance. We theoretically optimize the heterostructure, optical cavity and electrical properties. The resistance of the device is reduced by a factor of ~6.5 compared to a design without a tunnel junction, which is a significant improvement in current injection efficiency. We also show that the Joule heating is reduced by 69%.

2.2. Epitaxial Heterostructure Design

The schematic of the nanolaser under consideration is shown in Figure 2-1. Figure 2-1(a) corresponds to the design [60] of an electrically pumped metallo-dielectric nanolaser (labeled "device-O") without a tunnel junction. The gain medium consists of an intrinsic 320-nm-thick bulk InGaAs lattice matched to InP, which was predicted to be more suitable than InGaAsP multiple quantum wells nanolasersin terms of reducing threshold and single mode operation [36] Highly doped InGaAsP layers ($2\times10^{19}cm^{-3}$) on the bottom and top are the electrical contacts and doped InP layers serve as cladding layers through which the current is injected into the active layer. The radius of the gain medium and the InGaAsP contact layers is 320nm. The 160-nm-undercut of the InP pedestals improves the mode quality factor, as discussed in [60]. The nanostructure is covered by an Al_2O_3 dielectric layer to improve the thermal management followed by the silver layer added to improve the confinement [37]. The bottom p-InGaAsP and p-InP layers are poor conductors limiting the current injection efficiency. Since the mobility of holes is much lower than electrons, a high applied voltage is needed for current injection which tends to increase the Joule heating. The current injection resistance can be reduced by incorporating a tunnel junction into the nanolaser structure, as shown in Figure 2-1(b). The tunnel junction consists of a heavily doped InGaAsP PN junction with 20-nm-thick p-InGaAsP and 12-nm-thick n-InGaAsP and it is placed below the p-InP ($1\times10^{18}cm^{-3}$) cladding layer.

The working principle of a tunnel junction is illustrated by a reduced band diagram and the junction IV curve, both shown in Figure 2-1(c). The doping concentration for both p- and n-type layers is $5\times10^{19}cm^{-3}$. Such high doping concentration enables the Fermi level under equilibrium to be above the conduction band for n-type and below the valence band for p-type material without any bias. Since the depletion region is now extremely narrow, when a negligible reversed bias is applied, the Zener Effect enables a tunneling current through the junction. Therefore it is a conductive layer under negligible reverse bias. It is worth mentioning that in both Figure 2-1(a) and (b) electrons are injected from the top and holes from the bottom which means when the device is under forward bias, the tunnel junction itself is under reverse bias.

It is worth to notice the IV curve of Figure 2-1(c) corresponds to an applied voltage on the tunnel junction (not the entire device). Therefore, when the device is under reverse bias, even though the tunnel junction is under forward bias, the device can behave as an insulator.

By incorporating the tunnel junction, we can replace the poorly conductive p-InGaAsP and p-InP (5×10^{18} cm^{-3}) layers by n-InGaAsP and n-InP (5×10^{18} cm^{-3}) layers respectively. However, heavily doped tunnel junctions are lossy layers due to free carrier absorption. Indeed, the position of the junction must be properly chosen to optimize the nanostructure performance. The total thickness of InP layers between the InGaAs gain medium and the top of bottom p-InGaAsP contact is 850nm. In Figure 2-1(b), we define a variable "d" representing the distance between the bottom of the gain media to the top of the tunnel junction. Below the tunnel junction, p-type layers are replaced by n-type ones. In the following we investigate the influence of the tunnel junction position upon the cavity mode, i.e. when the tunnel junction is positioned at d=125nm (design labeled “-TJ-125”) and d=725 nm (design labeled “-TJ-725”) from the optical mode.

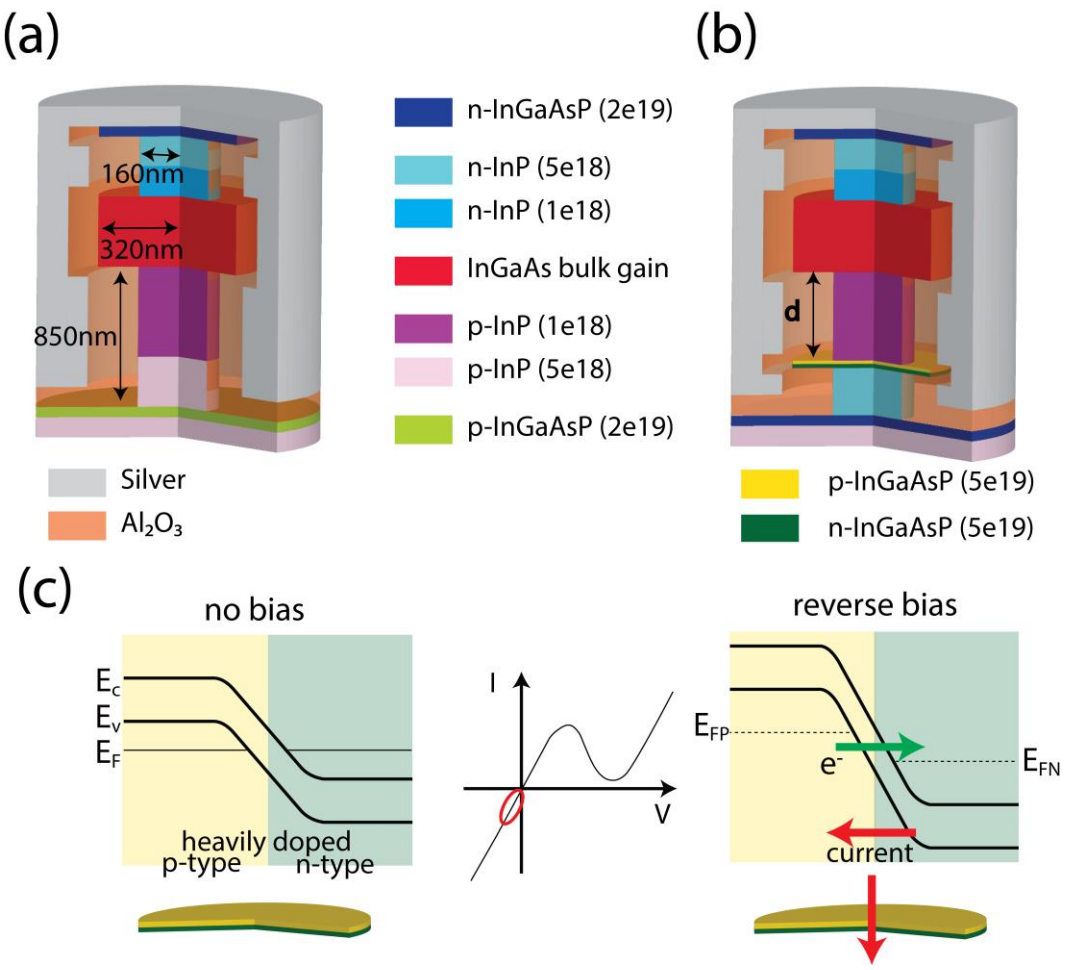

Figure 2-1 Schematics of nanolasers (a) without and (b) with tunnel junction. (c) Reduced band diagram of a tunnel junction with no bias and reverse bias, and the respective IV curve. E_C is the conduction band and E_V is the valence band. E_F, E_{FP} and E_{FN} are the Fermi level, quasi-Fermi level for holes and quasi-Fermi level for electrons, respectively.

A small resistance is expected with the device-TJ-125 but at the cost of a lower quality factor because of the mode overlap with the tunnel junction. In contrast, device-TJ-725has a lower overlap of the optical mode with the lossy tunnel junction layer increasing the quality factor of the optical mode. A more detailed analysis is addressed in the next section.

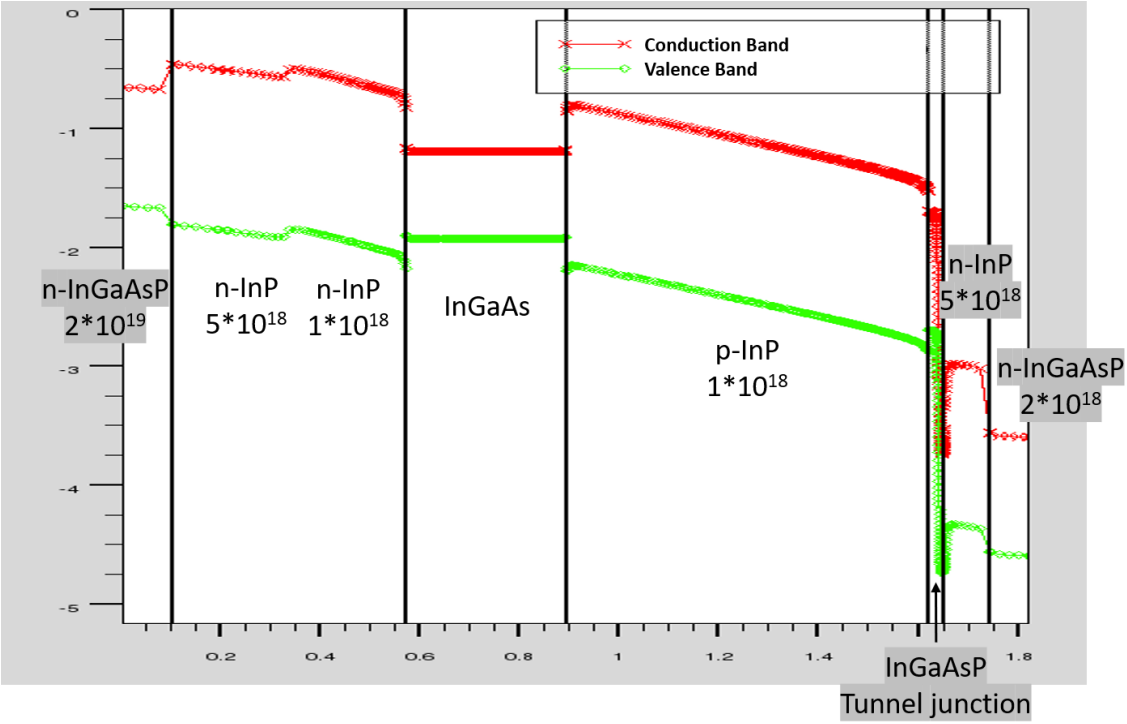

Figure 2-2 Band diagram of the tunnel junction incorporated tunnel junction under forward bias. (The material composition of each layer and doping concentration (cm^{-3}) are shown)

Figure 2-2 shows the band diagram of the tunnel junction incorporated nanolaser under forward bias. The middle intrinsic InGaAs is the gain material where the optical carrier generation and recombination taking places. InP layers on both side of the InGaAs serve as separate confinement heterostructure (SCH) layers to achieve better carrier confinement. N-InGaAsP on both ends are the contact layers. The tunnel junction is a 32nm thin InGaAsP p-n junction. The electrons in the valence band of the p-InP tunnel through the tunnel junction and reach n-InP and n-InGaAsP on the right side.

2.3. Optical Cavity

To calculate the quality factor and confinement factor of the nanolasers, 3D simulations were carried out using the commercial FEM software (COMSOL). Usually the imaginary part of

the refractive index (κ) is considered for metals but neglected for semiconductor and dielectrics because its values are much lower. However, the heavily doped tunnel junction is a highly absorbing layer due to its free carrier absorption. If κ is not considered, the simulated Q can be overestimated and consequently the calculated g_{th} is underestimated.

Therefore, we employ the Drude (plasma) model to determine the loss, α, and κ, which are related by the expressions: [61]

$$\Delta\alpha = \left(\frac{q^3\lambda^2}{4\pi^2 c^3 \varepsilon_0 n}\right)\left[\frac{\Delta N_e}{m_{ce}^{*2}\mu_e} + \frac{\Delta N_h}{m_{ch}^{*2}\mu_h}\right] \quad (1)$$

$$\kappa = \frac{4\pi\alpha}{\lambda} \quad (2)$$

where q is the electronic charge, c is the speed of light, ε_0 is the vacuum dielectric permittivity ,n is the real part of the refractive index of the unperturbed material, $m^*_{ce/h}$ is the effective mass of electrons/holes, $\mu_{e/h}$ is the electron/hole mobility and $\Delta N_{/eh}$ is the electron/hole carrier density. The undoped InP and InGaAsP are considered transparent at the bulk gain media emission wavelength, so the free carrier absorption accounts for the loss just in the doped absorbing layers.

In equation (1), we have also considered a carrier dependent mobility model for electrons and holes. This model is described in detail in [62] as expressed as

$$\mu_{LF}(N,T) = \mu_{min} + \frac{\mu_{max}(300k) - \mu_{min}}{1 + \left(\frac{N}{N_{ref}(300K)}\right)^{\lambda}} \quad (3)$$

At very high doping concentration, mobility saturates at μ_{min} , which is temperature independent and at very low doping concentration, mobility saturates at μ_{max}, the lattice-limited mobility. N_{ref} (300K) is the doping concentration at which mobility reduces to almost half of its

maximum value at low doping. Linear, or quadratic interpolations are used to determine the InGaAs and InGaAsP. The parameters are listed in Table 2-1

Table 2-1 Fitting parameters for the low-field mobility model [62]

Material	Electron or Hole	μ_{max} (300K) ($cm^2/V\ s$)	μ_{min} ($cm^2/V\ s$)	N_{ref} (300K)	λ
InP	Electron	5200	400	3×10^{17}	0.47
	hole	170	10	4.8×10^{17}	0.62
GaAs	Electron	9400	500	6×10^{16}	0.394
	hole	491	20	1.48×10^{17}	0.38
InAs	Electron	34000	1000	1.1×10^{18}	0.32
	hole	530	20	1.1×10^{17}	0.46
GaP	Electron	152	10	4.4×10^{18}	0.8
	hole	147	10	1×10^{18}	0.85
$In_{0.53}Ga_{0.47}As$	Electron	14000	300	1.3×10^{17}	0.48
	hole	320	10	4.9×10^{17}	0.403

For the quaternary material $In_{1-x}Ga_xAs_yP_{1-y,}$ to determine the $\mu_{p,min}$, $\mu_{n,max}$ (300K), Log10[$N_{n,ref}$ (300K)], Log10[$N_{p,ref}$ (300K)] and λp, the following interpolation scheme is used [62]

$$\mu\left(In_{1-x}Ga_xAs_yP_{1-y}, 300K\right) = \frac{y\mu(In_{1-x}Ga_xAs, 300K) + (1-y)\mu(In_{1-x}Ga_xP, 300K)}{1 + my(1-y)} \quad (4)$$

with m=6

For other parameters the following equation is used

$$\lambda\left(In_{1-x}Ga_xAs_yP_{1-y}\right) = y\lambda(In_{1-x}Ga_xAs) + (1-y)\lambda(In_{1-x}Ga_xP) \quad (5)$$

As for the parameters for $In_{1-x}Ga_xAs$ and $In_{1-x}Ga_xP$, InAs, GaAs, InP and GaP are used for linear interpolation.

Figure 2-3(a) and Figure 2-3(b) show the electron and hole carrier density dependent mobility. It can be seen that the carrier mobility decreases when increasing doping concentration. Figure 2-3(c) shows the calculated κ for InP and InGaAsP. The tunnel junction doping concentration of $5\times10^{19}cm^{-3}$results in a κ of 0.014 and 3.64×10^{-4} for the p-InGaAsP and n-InGaAsP layers, respectively. The mode overlap with the p-InGaAsP layer is then expected to decrease the Q-factor of the optical mode.

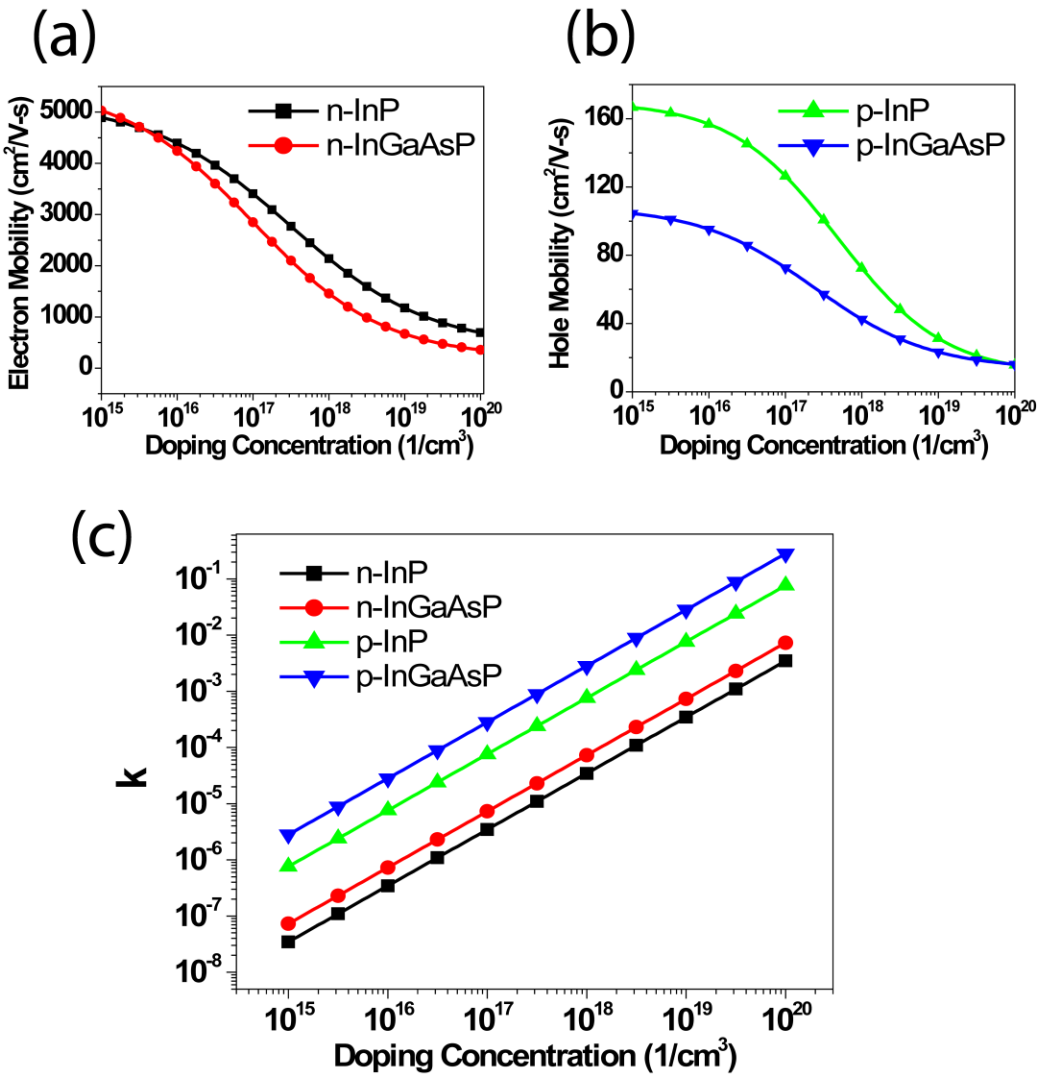

Figure 2-3 Calculated (a) electron and (b) hole mobilities for n- and p- doped InP and InGaAsP, respectively, and the(c) imaginary part of their refractive index (κ) for the different doping concentrations.

We performed 3D simulations by placing the tunnel junction beneath the gain media by d=725nm and d=125nm. Figure 2-4 shows the electric field of the lowest threshold mode, TE_{012}, at a resonant wavelength within the material gain bandwidth and in the telecom C-band. The mode profile of a nanolaser without tunnel junction (device-O) is shown in Figure 2-4 (a). Figure 2-4 (b) and Figure 2-4(c) are the nanolasers consisting of tunnel junctions with d=725nm and d=125nm, respectively (device-TJ-725 and device-TJ-125). The Q-factor, resonant wavelength (λ),

confinement factor (Γ) and threshold gain (g_{th}) calculated as in [37] are also presented. If the tunnel junction is placed far enough from the gain media(device-TJ-725), shown in Figure 2-4(b), the mode properties do not change significantly. In fact, Γ (0.325) and g_{th} (339.6 cm^{-1}) are superior than device-O. In Fig. 3(c) the optical mode is pulled down compared with Fig. 3(a) due to the high index InGaAsP tunnel junction. Γ drops from 0.307 to 0.287 and the mode overlap with the heavily doped tunnel junction also increases the loss resulting in lower Q and higher g_{th}, which increases from 363.8 cm^{-1} to 878.5 cm^{-1}.

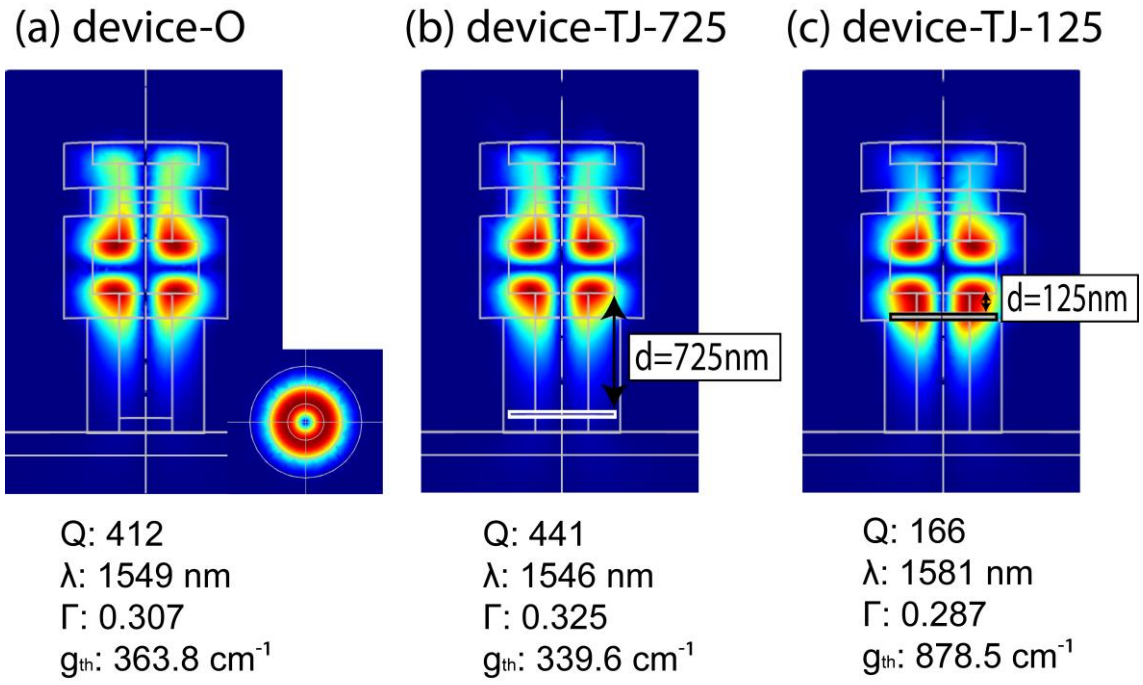

Figure 2-4 Electric field of the lowest threshold mode, TE_{012}, for a nanolaser (a) without tunnel junction (device-O), (b)with a tunnel junction at d=725nm(device-TJ-725) and (c)with a tunnel junction at *d*=125nm (device-TJ-125)

2.4. Laser Rate Equations

To obtain the threshold carrier density we then solve the laser rate equations, which are expressed as[63]:

$$\frac{dN}{dt} = R_{pump} - R_{sp} - R_{sur} - v_g gP \tag{6}$$

$$\frac{dP}{dt} = \Gamma v_g gP + \Gamma \beta R_{sp} - \frac{\omega}{Q} P \tag{7}$$

Where N is the carrier density, P is the photon density, R_{pump} is the pump rate by electronic injection, v_g is the group velocity, R_{sp} is the spontaneous emission rate and g is the material gain [64] where the detail of calculation can be found in[63]. R_{sur} is the surface recombination rate which is critical to high surface to volume ratio nanoscale devices. The surface recombination velocity is assumed to be $5x10^4$ cm/s for InGaAs lattice matched to InP [36], β is the spontaneous emission coupling factor and ω is the resonance frequency, which is extracted from COMSOL simulations in Figure 2-4.

2.4.1. InGaAs Gain spectrum

The optical gain as a function of wavelength can be calculated from the equation

$$\mathrm{g}(\omega; \mathrm{N}; \mathrm{T}) = \frac{\pi\, q^2}{n_r \epsilon_0 c m_0 \omega} \int |M_T(E_{21})|^2\, \rho_r(E_{12}; T)[f_2(N; T) - f_1(N; T)]\ \mathrm{d}E_{21} \tag{8}$$

q is the fundamental charge, nr is the refractive index, ε_0 is the vacuum permittivity, c is speed of light, m_0 is the free electron mass, ω is the frequency, M_T is the transition matrix element, ρ_r is the density of state and f_2 and f_1 are Fermi distributions.

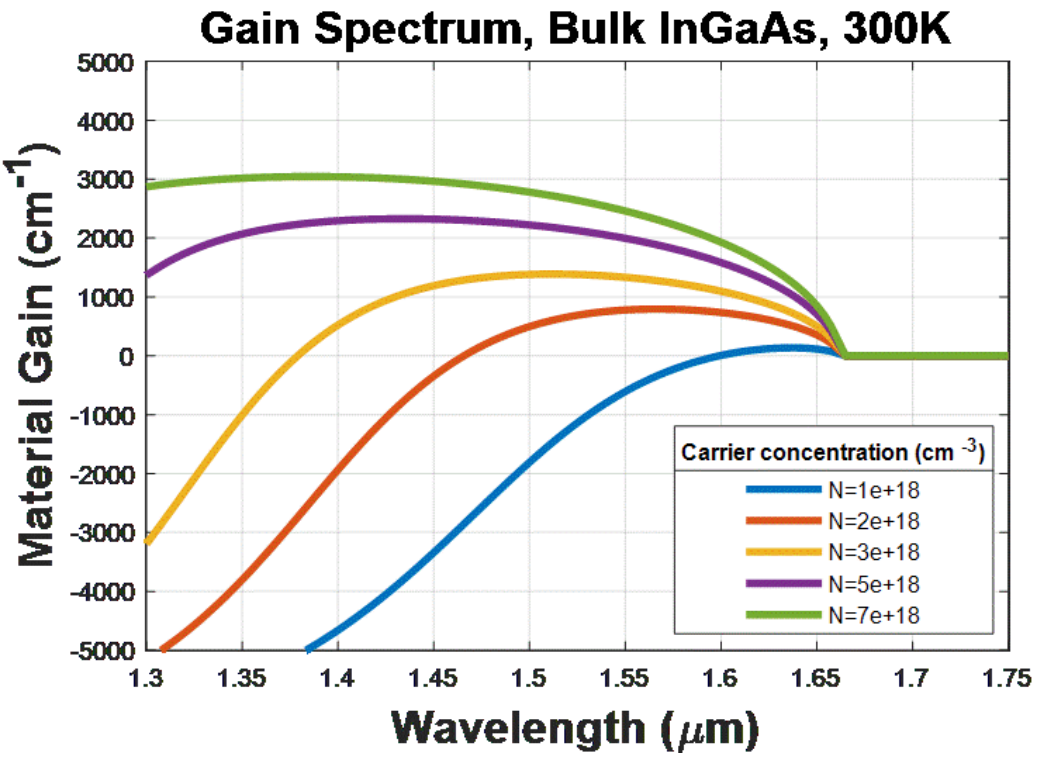

Figure 2-5 Gain Spectrum of InGaAs

In Figure 2-5 we plot the gain over the wavelength range of 1.3 μm <λ< 1.75 μm at T = 300 K with carrier concentration (N) as a parameter. When carrier concentration is above $2*10^{18}(1/cm^3)$, the material is above transparent over the C-band where the laser emission wavelength is. The material gain at the emission wavelength with respect to the carrier concentration N will be used in the laser rate equation.

2.4.2. InGaAs spontaneous emission spectrum

The spontaneous emission spectrum is given by

$$\mathrm{R}_{sp}(\omega;\mathrm{N};\mathrm{T}) = \frac{4}{3}\frac{\pi\, q^2\omega}{n_r\epsilon_0 hc^3 m_0^2}\int |M_T(E_{21})|^2\, \rho_r(E_{12};T) f_2(N;T)[1 - f_1(N;T)]\, \mathrm{d}E_{21} \tag{9}$$

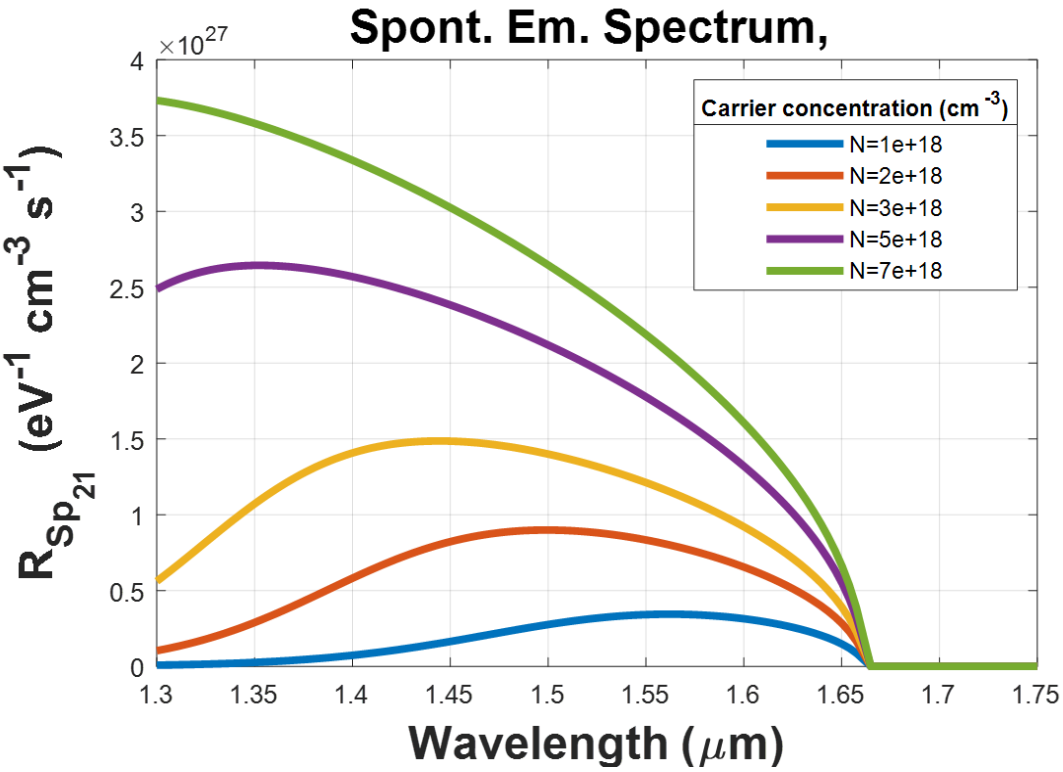

Figure 2-6 spontaneous emission Spectrum of InGaAs

In Figure 2-6, we plot the spontaneous emission similarly to the gain of Figure 2-5. The spontaneous emission with respect to the carrier concentration N will be used in the laser rate equation.

2.4.3. Threshold carrier concentration

Figure 2-7 shows the calculated carrier and photon density as a function of R_{pump} in steady state. For nanolasers without a tunnel junction (device-O), the threshold carrier density is found to be 3.5×10^{18} (cm^{-3}), while a tunnel junction 725nm below the gain region(device-TJ-725) reduces the threshold carrier density to 3.05×10^{18} (cm^{-3}). Figure 2-7(b) shows that the slope efficiency for device-TJ-725 is higher than for device-O. However, a tunnel junction close to the gain region

presents (device-TJ-125) a very high threshold due to the lower quality factor induced by free-carrier absorption. These results illustrate the importance of where to place the tunnel junction. With proper design, the threshold carrier density could be comparable or even better than without the tunnel junction.

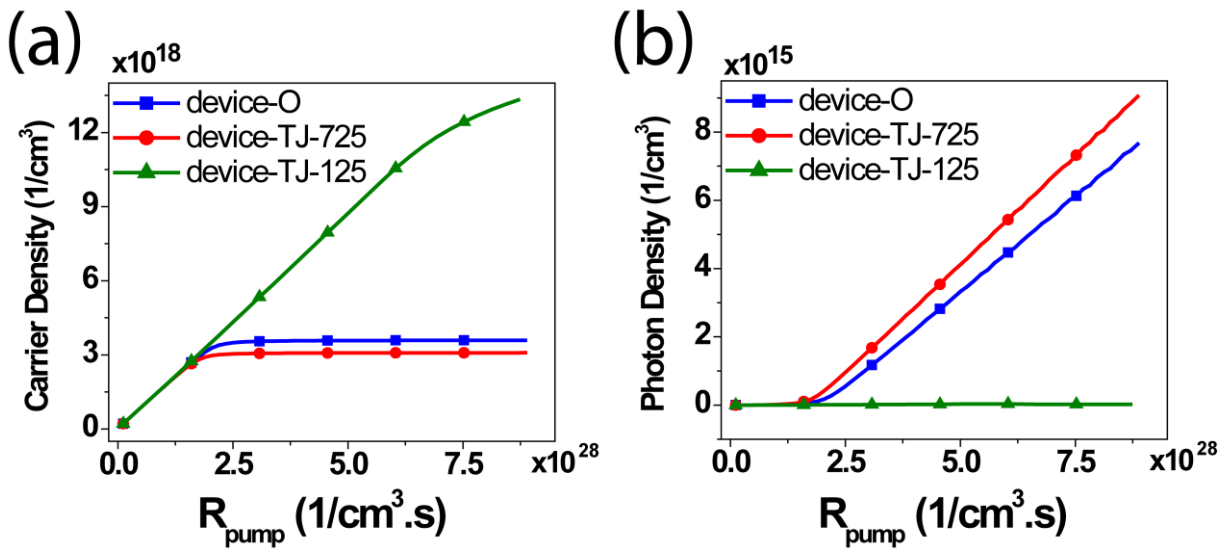

Figure 2-7 (a) Carrier density and (b)output photon density evolution with the injection pumping rate for the three designs in consideration.

2.5. Current Injection behavior

To understand how tunnel junctions reduces the resistance, threshold voltage, and current, we used the commercial software SILVACO's ATLAS to predict the current injection through the heterojunction. SILVACO self-consistently solves the Poisson equation, the Schrodinger equation, and the carrier transport equations considering Fermi-Dirac statistics. We assumed perfect ohmic contacts for current injection, and the carrier density dependent mobility model (shown in Figure 2-3(a) and (b)) was also incorporated into our simulations.

Figure 2-8(a) shows the simulated IV curve. Device-TJ-725 outperforms device-O because of the low hole mobility, which impairs the current injection on device-O. Indeed, once a tunnel junction is introduced, the bottom p-InGaAsP contact is replaced by n-InGaAsP. Also, part of p-InP layer is replaced by n-InP (see Figure 2-1(b)). Because the electron mobility is two orders of magnitude larger than the hole mobility, to reach the same current, a much lower applied voltage is needed for device-TJ-725.The high resistance from p-type layers can be minimized; the device resistance is 3372Ω for device-O and 519Ω for Device-TJ-725. Therefore the tunnel junction reduces the injection current resistance by ~6.5 times.

From SILVACO, we can also extract the carrier density in the gain region with respect to applied voltages as shown in Figure 2-8(b). To predict the threshold current, we related the results from laser rate equations to SILVACO simulations. In Figure 2-7, we have solved the rate equations at steady state to obtain the threshold carrier density for device-O ($3.5\times10^{18}cm^{-3}$) and device-TJ-725 ($3.05\times10^{18}cm^{-3}$). In Fig. 5(b), for device-O, 3.05V is required to reach lasing threshold at room temperature. For device-TJ-725, which has n-InGaAsP on both ends as contact layers, only 1.35V is needed to reach lasing threshold.

Figure 2-8(c) shows the relation between the carrier density in the gain region and the current. The threshold current for device-TJ-725 is reduced by 31% compared to device-O. The two curves are almost identical below and above the threshold carrier density which means the reduced threshold current of device-TJ-725 results from a lower threshold carrier density.

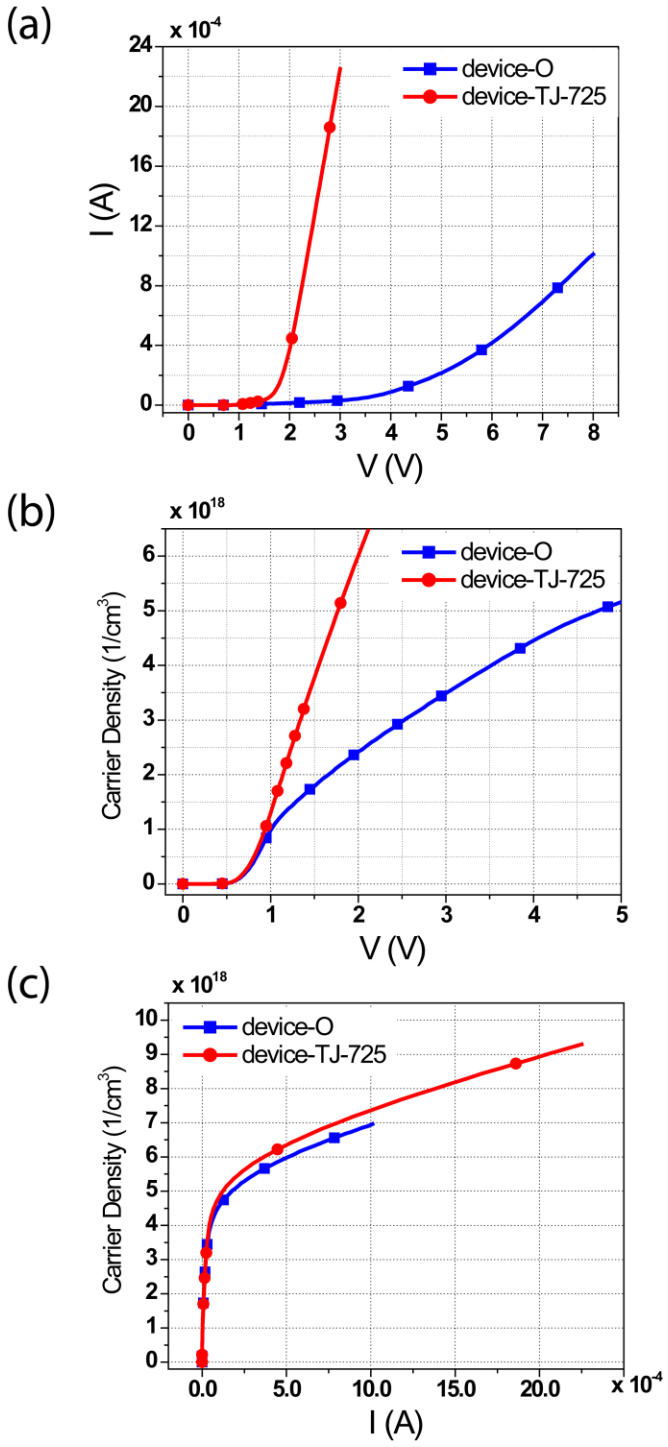

Figure 2-8 (a) IV curve and (b) carrier density in the gain medium vs. applied voltage. (c) Carrier density in the gain medium vs. injection current.

2.6. Discussion

Inserting a heavily doped tunnel junction reduces the threshold voltage by 55% and current by 31%, leading to 69% reduction in power consumption and Joule heating. Room temperature nanolasers always suffer from self-heating due to the current injection. We had already proposed using Al_2O_3 instead of SiO_2 as the cladding layer for thermal management [37]. By incorporating a tunnel junction, thermal management can be further improved, which is necessary to realize stable room temperature nanolasers.

To optimize the structure, optimizing tunnel junction location is essential. Therefore understanding how "*d*" in Figure 2-1(b) changes the cavity property and current injection is necessary in our design. We summarize the laser parameters in Table I. Optical characteristics calculated from COMSOL including Q, λ, Γ and g_{th} are listed; threshold carrier density (N_{th}) from laser rate equations and threshold applied voltage (V_{th}) from SILVACO are also presented.

Table 2-2 shows the lossy tunnel junction position can be detrimental to the optical mode. The closer it is to the gain medium (smaller d), the smaller the Q is. On the other hand, placing a tunnel junction close to the gain region can reduce the amount of p-type layers and reduce the device resistance. There is indeed an inherent trade-off between the resistance and Q reduction as d is decreased. As an example, for device with d= 325nm, V_{th} is 1.65V which is 0.3V higher than that with d= 725nm, showing that the resistance reduction does not compensate the Q reduction. Therefore, placing a tunnel junction far enough from the gain media is ideal to prevent optical mode overlap with the lossy layer for our metallo-dielectric nanolasers.

Table 2-2 Simulated laser characteristics forthe lowest threshold gain mode of devices with different "d"

d (nm)	Q	λ (nm)	Γ	g_{th} (cm^{-1})	$N_{th}\times10^{18}$ (cm^{-3})	V_{th} (V)
125*	166	1581	0.287	878.5	X	X
325	290	1551	0.306	519.6	5.9	1.65
525	389	1546	0.319	385.0	3.6	1.4
725*	441	1546	0.325	339.6	3.05	1.35
Device-O	412	1549	0.307	363.8	3.5	3.05

d=125nm is device-TJ-125; d=725nm is device-TJ-725;

We also analyzed the tunnel junction doping concentration influence on the threshold voltage and Joule heating. We considered only the optimized device-TJ-725, but with tunnel junction doping concentrations of 5×10^{18} cm^{-3}, 1×10^{19} cm^{-3} and 2×10^{19} cm^{-3}. Since the tunnel junction is 725nm below the gain region, the mode overlap with the tunnel junction was neglected. Therefore, we assume Q, Γ and g_{th} do not change with the doping concentration of the tunnel junction in this case. The calculated threshold voltage are then 2.4V, 1.75V and 1.5V, reducing the Joule heating by 44%, 60% and 62% respectively. These results show tunnel junctions are reliable even for lower doping concentrations.

2.7. Summary

In this article, we have analyzed the effect of incorporating a tunnel junction into our metallo-dielectric nanolasers. We proposed a new epitaxial structure and conducted optical and electrical modeling to theoretically demonstrate that electrical resistance of the device can be reduced without sacrificing the optical properties. By replacing the p-contact to form a PN tunnel junction 725nm below the gain medium, the device resistance is reduced by a factor of ~6.5. The applied threshold voltage is reduced from 3.05V to 1.35V and the threshold current by 31%, which results in a 69% reduction in Joule heating whereas the threshold gain for devices with and without tunnel junctions are comparable.

Chapter 2, in part, is a reprint of the material as it appears "Low resistance tunnel junctions for efficient electrically pumped nanolasers. " Fang, C. Y., Vallini, F., El Amili, A., Smalley, J. S., & Fainman, Y. (2017). *IEEE Journal of Selected Topics in Quantum Electronics*, 23(6), 1-6. The dissertation author was the primary coinvestigator and coauthor of this paper.

Chapter 3. Lasing Action in Tunnel Junction based Nanolaser

3.1. Introduction

Nanoscale cavity lasers have drawn considerable attention in the past decades to meet the needs of various applications [65] including optical interconnects for densely-packed chip-scale photonic circuits [66], [67], high speed modulation with low power consumption [68], sensing [69]–[71], and nonlinear optical microscopy [72].

The challenges in construction of nanolasers lie in co-design of optical cavity and electrical injection. For a cavity with sub-wavelength dimensions, the optical mode expands beyond its physical boundaries which dramatically increases radiative loss and lasing threshold. To address this issue, using metal is an excellent option because it can confine the optical mode into a small active volume and increases the overlap between the optical mode with the gain media. This approach has been demonstrated with different cavity designs such as plasmonic lasers [13], nano-bowties [73] and spasers [35]. However, optical mode overlap with metal also induces large optical loss and, consequently, decreases the quality factor of the resonator. To mitigate the metal loss, metallo-dielectric nanolasers were developed [29], where a combination of a dielectric shield and a metal layer, provides both large mode confinement and simultaneously reduces the metal loss. In the past, metallo-dielectric nanolasers with bulk InGaAsP [30] and multiple quantum wells of InGaAsP [74] as the gain medium have been demonstrated. A dielectric layer was deposited onto the semiconductor pillar and overcoated by a layer of Ag. The outer Ag layer increases the mode confinement while the inner dielectric layer reduces the mode overlap with the lossy metal and

also serves as an electrical insulation and passivation layer. More details on metallo-dielectric nanolaser designs can be found in [29], [30], [74].

Most of the reported studies on nanolaser structure designs use optical pumping. However, it is evident that electrical pumping is an essential step to make nanolasers useful for practical applications. Studies dedicated to injecting current into a small active region have been shown such as photonic crystal [12], gap plasmon [75] metal-clad cavities [38], [76] and metallo-dielectric nanolasers [31], [37] The latter uses current injection through contacts to P++ and n++ doped InP layers. However, their small physical dimensions and challenge in making low resistance p++ contacts still make current injection a major challenge. These large resistances lead to prohibitively high threshold voltage and current density of such nanoscale devices in comparison to larger scale semiconductor lasers. As a result, the Joule heating prevents the development of more efficient nanolasers.

A potential solution for more efficient current injection is to incorporate a tunnel junction and thereby decrease the resistance. A tunnel junction is formed by a heavily doped p-n junction. When a negligible reversed bias is applied, the Zener effect enables a tunneling current through the junction. The presence of a tunnel junction allows the current to be injected from n-type semiconductor layer from both sides (N-(NP)-PIN) rather than typical n-type on one side and p-type on the other side (PIN). Therefore, top and bottom metal semiconductor ohmic contacts are formed with the same metal and annealing process which reduces the fabrication complexity [77]. Moreover, tunnel junctions can replace some p-type material with n-type in the device. Because of the low electrical conductivity of p-type materials, the use of tunnel junction decreases the device resistance which therefore leads to the reduction of threshold voltage while alleviating the Joule heating [78]. The tunnel junctions have been used in the past to improve the current injection

efficiency of various large scale devices such as vertical cavity surface-emitting lasers (VCSELs) [52], [55, p.], light emitting diodes (LEDs) [54] and SOI-integrated InP-based micro lasers [58], [59] but have so far not been demonstrated in nanolasers.

In this manuscript, we experimentally demonstrate lasing action in tunnel junction incorporated into electrically pumped metallo-dielectric nanolasers. The presence of tunnel junction reduces the resistance leading to reduction of threshold voltage from 5V [19, 20] to less than 1V at 77K. We also conduct second-order coherence ($g^{(2)}(\tau)$) measurement to confirm the lasing behavior. Compared to metallo-dielectric nanolasers without tunnel junctions, the new structure suffered less Joule heating and lase up to 180K.

3.2. Fabrication

The schematic diagram of the nanolaser is shown in Figure 3-1. The nanolaser is based on an InP/InGaAs/InP double heterostructure grown on an InP wafer. The epitaxial heterostructures are grown by molecular beam epitaxy (MBE). The gain material is a 320nm thick intrinsic bulk InGaAs layer lattice matched to InP [36]. The top and bottom layers where the metal ohmic contacts are deposited are n-InGaAsP. The tunnel junction, which consists of heavily doped 20nm p-InGaAsP (dopant: Be) and 12nm n-InGaAsP (dopant: Si) lies beneath the p-InP layer. The tunnel junction doping concentrations for p-InGaAsP and n-InGaAsP are 4×10^{19} cm^{-3} and 4.7×10^{19} cm^{-3}, respectively. InP layers between gain and InGaAsP layers serving as electron and hole transport layers are under-cut to achieve better vertical mode confinement[60].

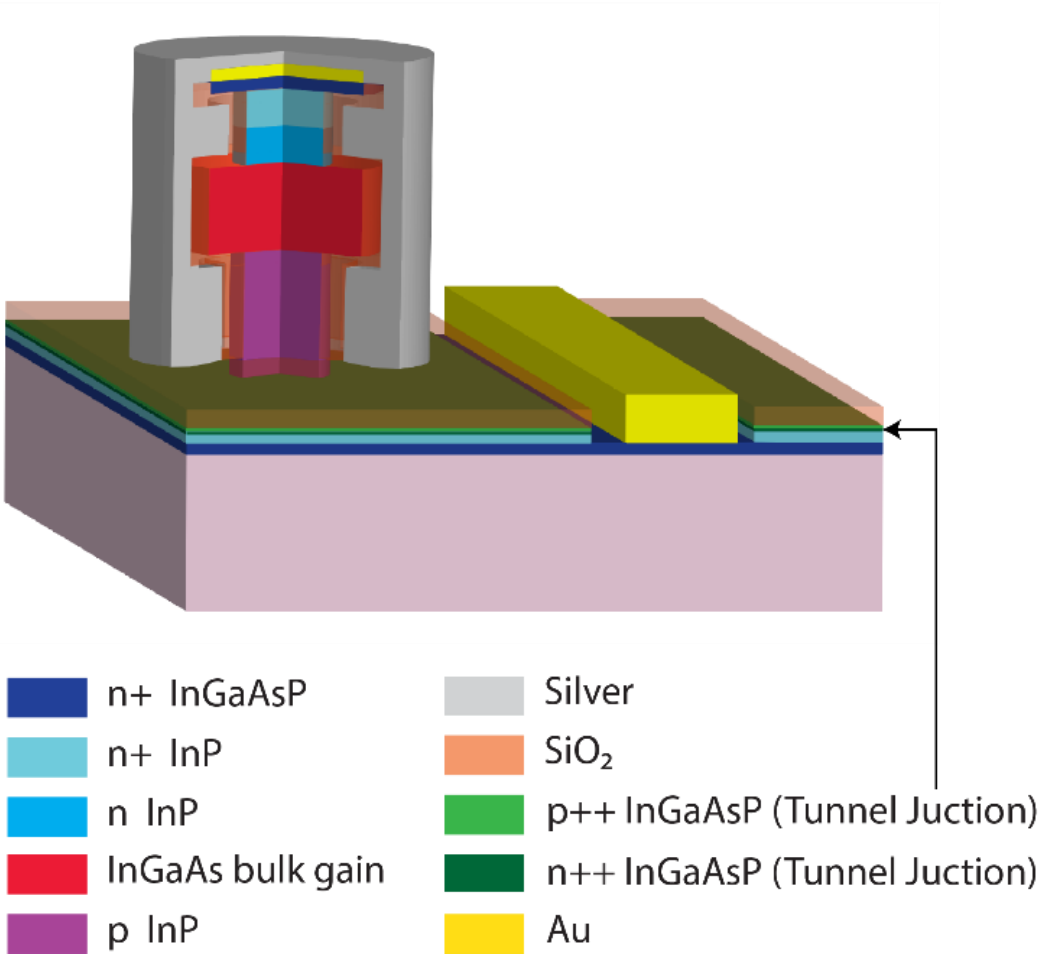

Figure 3-1 Schematic of tunnel junction incorporated nanolaser (The position of the tunnel junction is indicated by the arrow).

To fabricate the nanolasers, electron-beam lithography with hydrogen silsesquioxane (HSQ) resist was used to define the geometry of the gain medium followed by reactive-ion etching (RIE) to form pillar structures. Figure 3-2(a) shows the SEM image after RIE. Selective wet etching was then performed to undercut the doped InP layers without etching InGaAs and InGaAsP layers (Figure 3-2(b)). After the removal of HSQ on top of the pillar, SiO_2 dielectric layer was then deposited to shield the pedestal through plasma-enhanced chemical vapor deposition (PECVD). Photo resist planarization and dielectric etching was then done to access the top n-InGaAsP contact layer (Figure 3-2(c)). The top electrodes (Ti/Pd/Au) were deposited by electron-beam evaporation and lift-off process. (Figure 3-2(d)) The bottom contact region was defined by photolithography

and opened by etching the p++/n++ InGaAsP tunnel junction, n-InP and SiO_2 layer. Afterwards, bottom electrodes (Ti/Pd/Au) and cavity metal (Ag) were formed through multiple photolithography, evaporation, sputterring, lift-off and thermal annealing processes similar to those described in [19, 20]. Figure 3-2(e) shows the *I-V* curve of the nanolaser. The device resistance is around 740Ω. While the nanolaser without a tunnel junction, the device resistance is over 8 kΩ [37]. The presence of a tunnel junction reduces the device resistance by an order of magnitude.

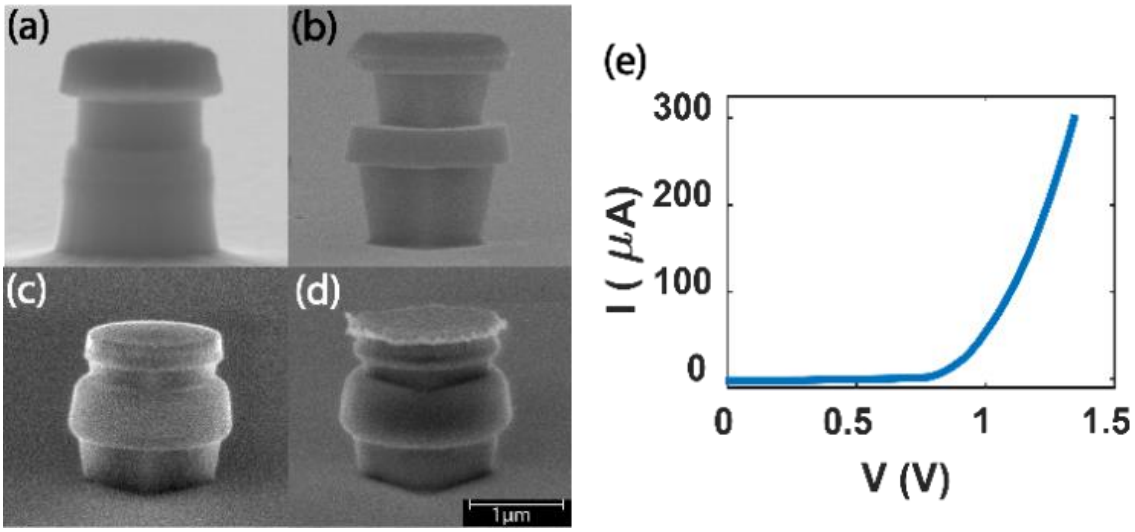

Figure 3-2 (a)-(d) SEM images of the nanolaser (a) after dry etching (b) after selective wet etching (c) after dielectric deposition (d) after top contact metal deposition. (e) the I-V curve of the nanolaser.

To verify the benefit of forming metal contact on n-type instead of p-type material, we conduct transfer length method (TLM) to measure the semiconductor/metal contact resistance of both n and p type InGaAsP layer with doping concentration of ~2×10^{19} (cm^{-3}). Our metal contact consists of 20nmTi, 20nmPd and 80nmAu layers followed by thermal annealing at 400°C. The experimental result shows contact resistance is 5×10^{-5} Ω·cm^2 on p-InGaAsP and less than 1×10^{-7}

$\Omega \cdot cm^2$ on n-InGaAsP. In this new nanolaser structure, bottom p-InGaAsP is replaced by the n-InGaAsP. Therefore, by forming both metal contacts on n-type instead of one on n-type and the other on p-type in the past, the contact resistance is reduced without increasing the fabrication complexity.

3.3. Laser characterization

Figure 3-3(a) shows the nanolaser (radius of 0.95μm) normalized emission spectrum at an ambient temperature of 77K with respect to different CW pumping current. Broadband spontaneous emission can be observed when the injection current is less than 5μA. As the injection current increases beyond 20μA, spectra narrowing can be observed. Above threshold, the lasing peak is located around 1540nm which is within the telecommunication wavelength regime.

To further validate lasing action, we conducted the light output versus injection current (L-I) characterization and measured the second-order coherence function $g^{(2)}(\tau) = \langle I(t)I(t+\tau)\rangle / \langle I(t)\rangle^2$ with a Hanbury Brown-Twiss (HBT) interferometer[79]. The measurement results are presented in Figure 3-3(b). The solid green dots show the L-I curve in log-log scale. The threshold current $I_{th,}$ defined by the inflection point of the kink in the LI-curve, is approximately 20μA. Furthermore, the second-order coherence function at zero delay, $g^{(2)}(\tau = 0)$, at various pump current is represented in Figure 3-3(b) by the blue dots. At pump current less than 20μA, the measured $g^{(2)}(\tau = 0)$ value is greater than 1, indicating that the device emission is incoherent. As the pump current increases toward 20μA, $g^{(2)}(\tau = 0)$ monotonically decreases correspondingly, signifying that the emission becomes more and more coherent. At pump current above 20μA, $g^{(2)}(\tau = 0)$ fluctuates around unity, suggesting that the emission is coherent and therefore, the device is operating in the lasing regime. Hence, the threshold current is also approximately 20μA according to our $g^{(2)}(\tau)$

measurement results. Therefore, the $g^{(2)}(\tau= 0)$ and LI-curve measurements are fully consistent with each other, which unambiguously confirms the lasing characteristics of our device.[80]

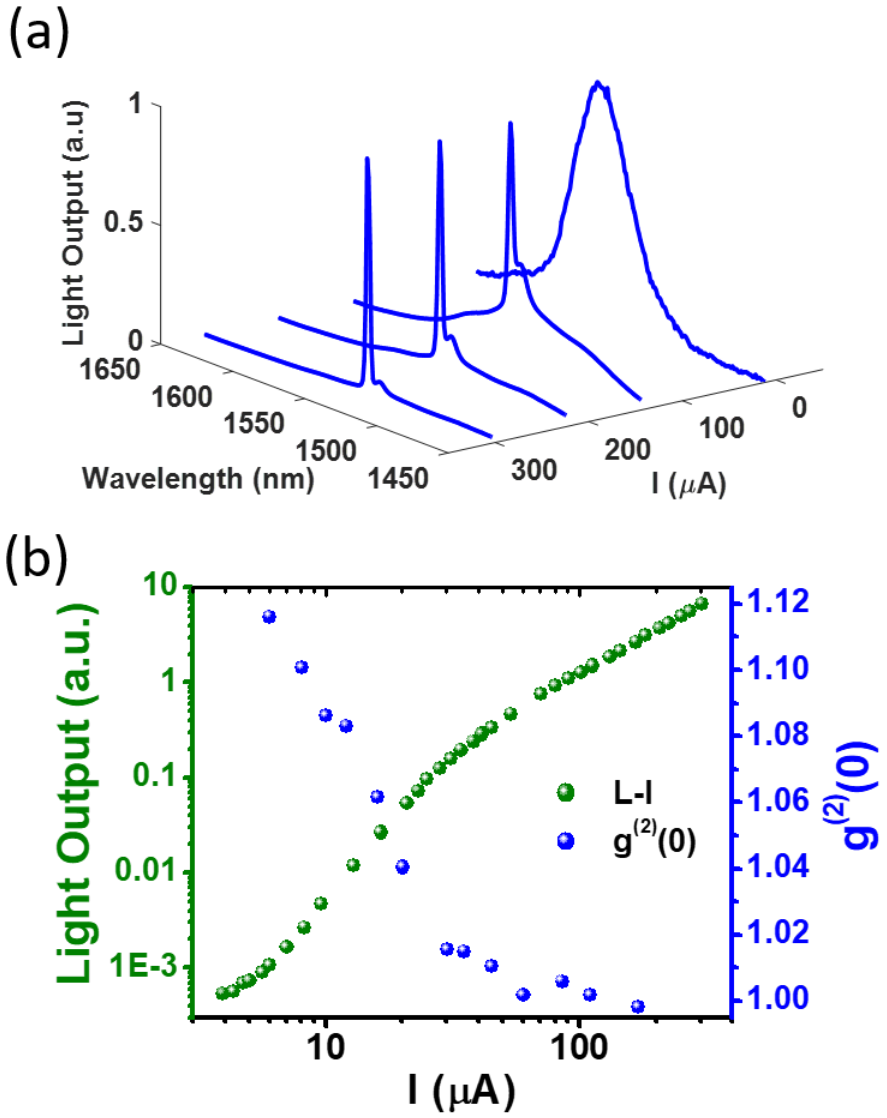

Figure 3-3 (a) Normalized emission spectral evolution of the nanolaser with increasing inject current at 77K. (b) (Green) The Light-current curve of the nanolaser. (Blue) The evolution of the nanolaser's second-order coherence function at zero delay g(2)(τ= 0).

The threshold current is mostly determined by the Q-factor of the optical cavity, so inserting a tunnel junction barely affects the threshold as long as the mode overlap with tunnel junction is minimized. By utilizing tunnel junctions, the voltage needed to achieve a certain current

level is decreased. Therefore, by reducing threshold voltage, Joule heating can also be reduced. The threshold voltage of the tunnel junction incorporated into nanolaser is around 0.95V compared to over 5V [19, 20] without utilizing it which means more than 80% reduction in Joule heating.

To further demonstrate that tunnel junction is capable of making nanolasers operational at higher temperature,we studied another nanolaser with the radius of 0.7 μm and the pillar height of 1.6 μm which leads to device dimension ~$0.59\lambda^3$. The spectra, L-I curve and linewidth evolution are shown in Figure 3-4. Figure 3-4(a) shows the emission spectrum an ambient temperature of 77K. The lasing peak is located at 1605nm and its linewidth is getting narrower as the current pumping increases. The temperature is then raised to 180K (Figure 3-4(b)). The linewidth narrowing is also observed at higher current with applied voltage less than 1.2V. The emission peak is located at 1610nm which means there is no mode hoping as the temperature increases. Figure 3-4(c) compares the *L-I* curves at 77K and 180K. A clear kink is observed which indicates that lasing behavior occurs at both temperatures. The threshold current at 77K is around 10μA and 100μA at 180K. The lasing threshold is higher at 180k due to reduction of semiconductor material gain compared to that at 77K. We also demonstrate the spectra linewidth evolution shown in Figure 3-4(d). The linewidth narrowing and reaching saturation above the threshold for both can be observed. At 77k the FWHM of the lasing peak is 0.5nm which corresponds to the quality factor of 3210. At 180K, the FWHM is 6nm at pumping current of 250 μA which is because of higher nonradiative recombination and decrease in material gain.

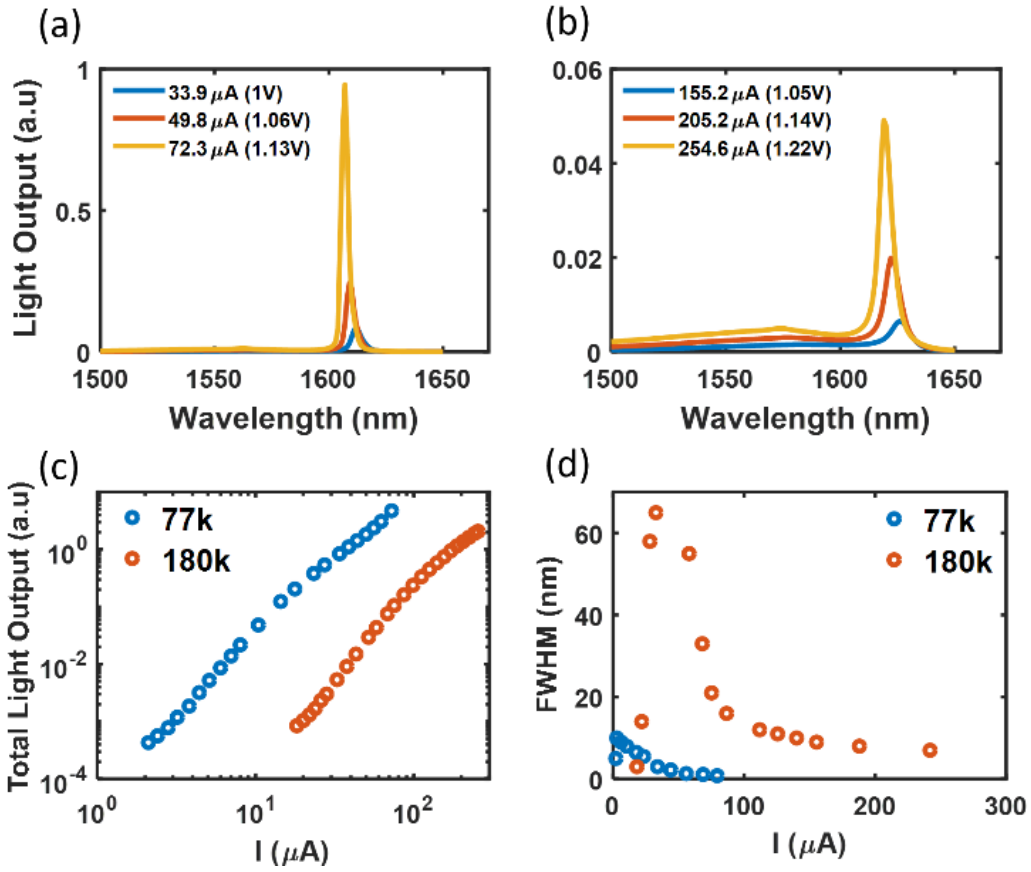

Figure 3-4 Emission spectrum of nanolaser (r=0.7μm) with different applied voltage and current at (a)77k, (b)180k and (c) The light-current curve (d) linewidth evolution of the lasing peak at 77k and 180k.

3.4. conclusion

In conclusion, we have experimentally demonstrated a new CW electrically pumped nanolaser where current is injected through n-type contacts on both sides of the device. The (N-(NP)-PIN) structure is formed by using a tunnel junction, a thin (less than 35nm) and heavily doped p-n junction. The presence of a tunnel junction reduced the device resistance by replacing the bottom p-type materials and forming better ohmic contacts. The experimental results show that the resistance is reduced and the threshold voltage is reduced from 5V to around 0.95V compared to

nanolasers without a tunnel junction. As a result, the Joule heating is alleviated. We prove the lasing action by showing L-I curve and second-order coherence function measurements ($g^{(2)}(\tau)$) under CW electrical pumping. Moreover, we have demonstrated that the metallo-dielectric nanolaser show lasing action at temperatures as high as 180 K because of better heat management. This work not only is beneficial to metallo-dielectric nanolasers but also paves the way for future application of tunnel junctions in other nanoscale optoelectronic devices.

Chapter 3, in part, is a reprint of the material as it appears "Lasing Action in Low Resistance Nanolasers based on Tunnel Junctions." Fang, Cheng-Yi, Si Hui Pan, Felipe Vallini, Antti Tukiainen, Jari Lyytikäinen, Gustav Nylund, Boubacar Kanté, Mircea Guina, Abdelkrim El Amili, and Yeshaiahu Fainman *(in submission)*. The dissertation author was the primary coinvestigator and coauthor of this paper.

Chapter 4. Microwave signal switching on a silicon photonic chip

Microwave photonics uses light to carry and process microwave signals over a photonic link. However, light can instead be used as a stimulus to microwave devices that directly control microwave signals. Such optically controlled amplitude and phase-shift switches are investigated for use in reconfigurable microwave systems, but they suffer from large footprint, high optical power level required for switching, lack of scalability and complex integration requirements, restricting their implementation in practical microwave systems. Here, we report Monolithic Optically Reconfigurable Integrated Microwave Switches (MORIMSs) built on a CMOS compatible silicon photonic chip that addresses all of the stringent requirements. Our scalable micrometer-scale switches provide higher switching efficiency and require optical power orders of magnitude lower than the state-of-the-art. Also, it opens a new research direction on silicon photonic platforms integrating microwave circuitry. This work has important implications in reconfigurable microwave and millimeter wave devices for future communication networks.

4.1. Background

Reconfigurability has become a crucial feature in modern, agile, microwave and millimeter wave (MMW) systems for emerging wireless communications, sensing and imaging.[81]–[85] Among various existing building blocks, optically reconfigurable MMW amplitude and phase-shift switches are key devises for beam steering in RADAR systems and reconfigurable antennas for emerging 5G wireless communications network [86], [87]. An optically controlled switch is a device whose electrical state can be tuned from insulating (Off state) to conductive (On state) by

means of optical stimuli [44], [45], [48], [88]. The underlying physics relies on photoconductive effect that occurs through the light interaction with a semiconductor material[39]. The illumination with a photon energy larger than the semiconductor bandgap generates electron-hole pairs in the control layer which modifies its electrical conductivity and affects the amplitude and phase of MMW signals.

The idea of using light to control or even introduce signals directly into microwaves devices [87], [89], [90] has drawn great interest in the microwave community driven by the need for dynamic control, fast response, immunity to electromagnetic interference, and good isolation between the controlling and controlled devices. The optical solution promises better performances compared to its classical analogue that utilizes electrical or microelectromechanical system which are prone to signal distortion and unwanted electromagnetic interferences.[81] Various reconfigurable microwave functionalities have been demonstrated including cognitive radio applications[90], microwave mixers [91] and phase shifters [92], [93]. Although optically controlled microwave amplitude and phase switches have attracted appreciable attention due to their superior potential performances, they are not yet sufficiently advanced for implementation in practical microwave systems. The main reasons are twofold: (i) lack of scalability and compactness due to the fact that current approaches use free-space or fiber illumination [49], [94] thus requiring costly and complex packaging and (ii) the optical power level required to perform a switching operation [45], [48], [95]–[97] is prohibitively high, e.g., to achieve On/Off RF switching with extinction ratio of ~10dB requires optical power in the range of tens to several hundreds of a milliwatts. Moreover, it should be noted that photodiode and phototransistors switches can operate at low optical power but they require electrical bias and are not scalable in

large high-frequency phased array systems.[98], [99] These challenges can be addressed by utilizing photonic technology to manipulating MMW signals in microwave systems.

In this manuscript we overcome these challenges and report the design, fabrication and experimental demonstration of Monolithic Optically Reconfigurable Integrated Microwave Switches (MORIMSs) built on a CMOS compatible silicon photonic chip**.** Silicon nitride waveguides are exploited to route optical waves towards silicon photoconductive patches to switch microwave signals at different locations of the chip. Photonic integration allows high light coupling efficiency into silicon photoconductive patches. We show that the integration of microwave circuits and optical waveguides on a CMOS platform provides scalable micrometer-scale footprint switches with higher switching efficiency, large phase shift and optical power requirement orders of magnitude lower than the state of the art. Our work paves the way for a new generation of complex optically reconfigurable microwave circuits that benefit from the integrated silicon photonics technology.

4.2. Device design

Emerging photonic integrated circuits (PICs) technology [100] has already made a significant impact on high-speed optical interconnects and digital optical communication links [101]. PICs manufacturing using silicon on insulator (SOI) platform is compatible with CMOS process allowing mass production at low cost[102]. It offers highly desirable features such as small footprint, scalability and reduced power consumption. By taking advantages of integrated photonics flexibility, our proposed devices use one single waveguide to control multiple microwave switches in different locations on the chip. Moreover, integrated photonics offers the possibility to engineer and optimize light coupling efficiency from optical waveguide to silicon photoconductive patches in order to achieve high switching performance. Depending on the

application, the microwave switches can also be addressed independently or combined with a variety of photonic building blocks such as Y-branch, directional couplers, ring resonators, Mach-Zehnder modulators, etc. With this vision in mind, we have developed two different MORIMS architectures as illustrated in Fig. 1a and b to meet different demands. Both architectures use a single mode silicon nitride (SiNx) waveguide, silicon (Si) photoconductive patch and aluminum (Al) co-planar waveguide transmission lines all built on the same SOI wafer. The signal electrode gap is made of a Si photoconductive patch that acts as an electrical insulator (Off state) but under illumination acts as a conductor (On state). The MORIMS operates with optical radiation at the wavelength of 808 nm.

The SOI wafer consists of 250nm-thick device layer and 3μm-thick buried oxide layer. During the fabrication process, most of the silicon material is removed to form Si photoconductive patches with dimension of 16μm by 12μm. Single-mode SiNx ridge waveguide with the dimensions of 800nm-width and 400nm-height are fabricated and used to guide light toward Si patches in order to activate them at different locations on the chip. The ridge waveguide and Si photoconductive patch are cladded by 1μm-thick SiO2 layer. The Ground-Signal-Ground (GSG) transmission lines consist of 800nm-thick Al lines with a tapered signal electrode toward the Si photoconductive patch.

The two proposed structures, referred as “tapered” and “through’ type, correspond to the way the optical waveguide is designed on top of the silicon photoconductive patch to optically control its conductivity. The “tapered type” structure (Figure 4-1(a)), where SiNx waveguide is tapered on the Si photoconductive patch, is devoted to maximizing the coupling of light from SiNx waveguide to Si photoconductive patch. The tapered-type structure allows ~84% of the energy to be coupled into the Si photoconductive patch. The “through type (Figure 4-1(b)), where waveguide

crossing the Si photoconductive patch, can be utilized in cascaded configuration, i.e., connecting "optically" different microwave circuits as it will be demonstrated later. Indeed, this configuration allows ~67% of the energy to be coupled into the silicon patch while the remaining light can be used to control the following microwave circuit. The details on both optical waveguide and transmission line designs are discussed in supplementary information section I and II.

Figure 4-1(c) and (d) show the SEM images of MORIMSs of both types. The SiNx waveguide conformally covers the Si photoconductive patch without any crack and discontinuity.

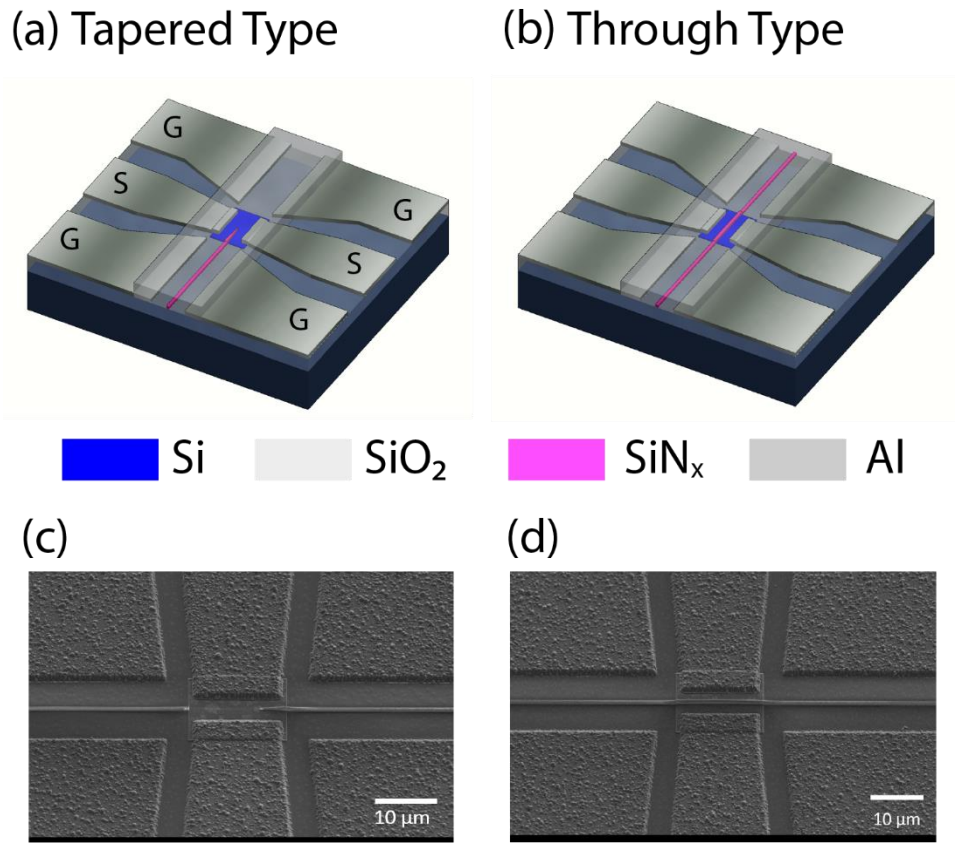

Figure 4-1 Schematic and SEM images of Monolithic Optically Reconfigurable Integrated Microwave Switches (MORIMSs). (a) Tapered type: SiNx waveguide tapered on top of photoconductive Si patch; (b) Through type: SiNx waveguide not tapered and connected to the output port. (c) side view SEM image of tapered type structure shown in Fig. 4-1a and (d) side view SEM image of through type structure shown in Fig. 4-1b.

4.2.1. Tapered- and through-type MORIMS design

To optimize the transfer of the light from the SiNx waveguide to the Si patch, finite-difference time-domain (FDTD, Lumerical©) simulations were conducted. In the tapered-type design, the SiNx is tapered along the Si patch while the waveguide is crossing it completely. Figure S1a and b show how the amplitude of the optical electromagnetic field is distributed within the Si patches in tapered-and through-type respectively. With the tapered type structure, the incident light can spread out laterally within Si photoconductive patch. On the contrary, through type structure, the electric field spreads less and its energy is exchanged coherently between the SiNx waveguide and the Si patch along the propagation direction. This configuration allows the remaining light to be re-used for controlling another MORIMS nearby as shown later. Figure S1c shows the fraction of optical power absorbed by Si photoconductive patch with different taper length. The tapered-type structure allows ~84% of the light to be coupled into the Si photoconductive patch. The length of the taper is one of the main parameters that governs the coupling efficiency between the waveguide and Si slab. For sake of comparison, through type structures allow ~67% of the energy to be coupled into the silicon patch.

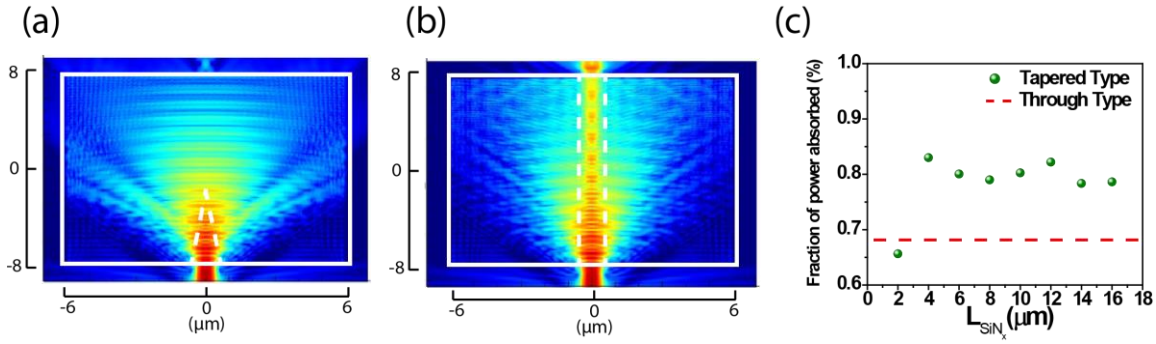

Figure 4-2 Computed local electromagnetic filed |E| distributions at the height of 125nm of (a) tapered type structure and (b) through type structure in the Si photoconductive patch. The white solid lines indicate the Si photoconductive patch and the dash lines depict the SiNx waveguide on top of the Si photoconductive patch. (c) Simulated fraction of power absorbed by Si photoconductive patch of tapered type structure and through type structure with different SiNx taper length.

4.2.2. Gap effect in Ground electrodes

The ground-signal-ground metal contacts on both ends are designed to match the 50 impedance of the probes that connect to the microwave source. The specialty in our design is that the input and output SiNx waveguide cut through the ground plane leaving a gap between them. To investigate the effect of these gaps in the ground planes, we simulate the s-parameter with different ground plane gap using CST Microwave Studio. The device design is the same as shown in Fig .1 except the gap width in the ground plane. Figure 4-3 shows the simulated S21 at both on and off states with different ground gap. At off state shown in Figure 4-3, where the intrinsic Si channel is not conductive, the S21 with different ground plane gap does not show significant difference. Figure 4-3b shows the simulated S21 at on state (with Si conductivity of 2000S/m). Although the different ground gaps show slight different S21, compared to the 20dB on/off ratio, the ground plane gap does not affect the device performance. Moreover, the microwave

wavelength is on the order of centimeter, so the micrometer scale ground plane gap does not play an important role in microwave signal transmission.

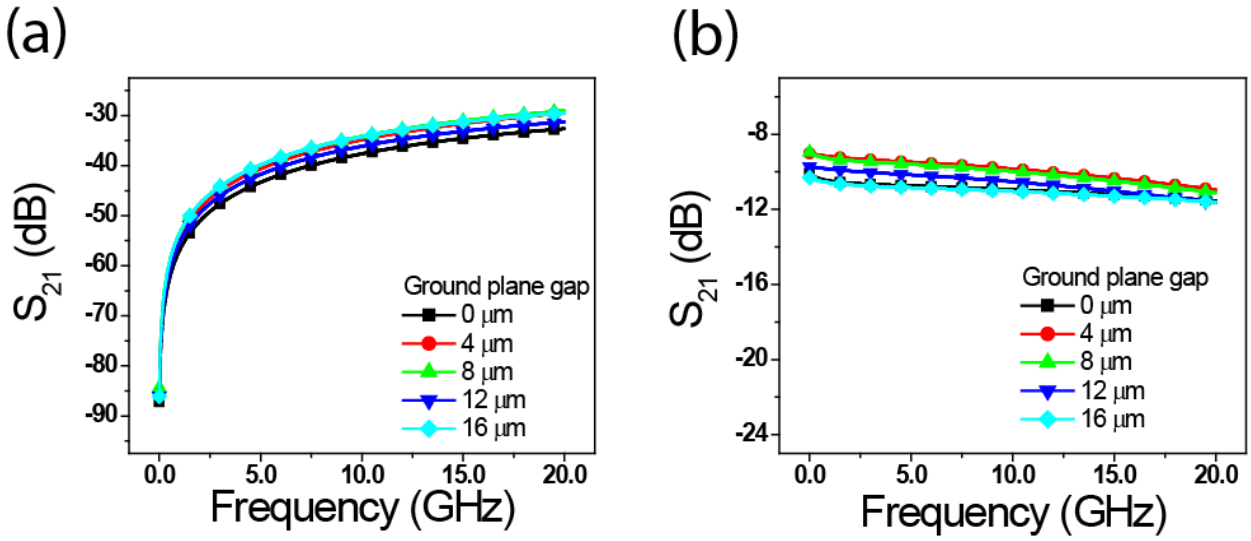

Figure 4-3 Simulated S21 with different ground electrodes gap of (a) off state and (b) on state.

4.3. Fabrication

MORIMSs are fabricated on an SOI wafer consisting of a 250nm- thick device layer and a 3μm thick buried oxide layer shown in Figure 4-4(a). The first step is to form Si photoconductive patch. 16μm by 12μm rectangle of hydrogen silsesquioxane (HSQ) was patterned through electron-beam lithography. Reactive ion etching (RIE) with gas mixture of SF_6 and C_4F_8 was used for silicon etching which is schematically shown in Figure 4-4(b). Next, the Al transmission lines were defined by another step of electron-beam lithography with PMMA as the resist followed by 800nm Al electron beam deposition. A lift-off process was then conducted to form the transmission line shown in Figure 4-4(c). To fabricate SiN_x waveguide, a 400nm thick SiN_x layer was deposited on top of the wafer through plasma-enhanced chemical vapor deposition (PECVD) shown in Figure 4-4(d). Electron-beam resist HSQ was then spun on and a lithography to form waveguides

was performed. After development, another RIE etching process with gas mixture of SF_6 and C_4F_8 was used to form the waveguide structure as shown in Figure 4-4(e). The waveguide is cladded by 1μm thick silicon oxide deposited using PECVD. The metal contact region was opened using photolithography and dry etching the SiO_2 layer shown in Figure 4-4(f).

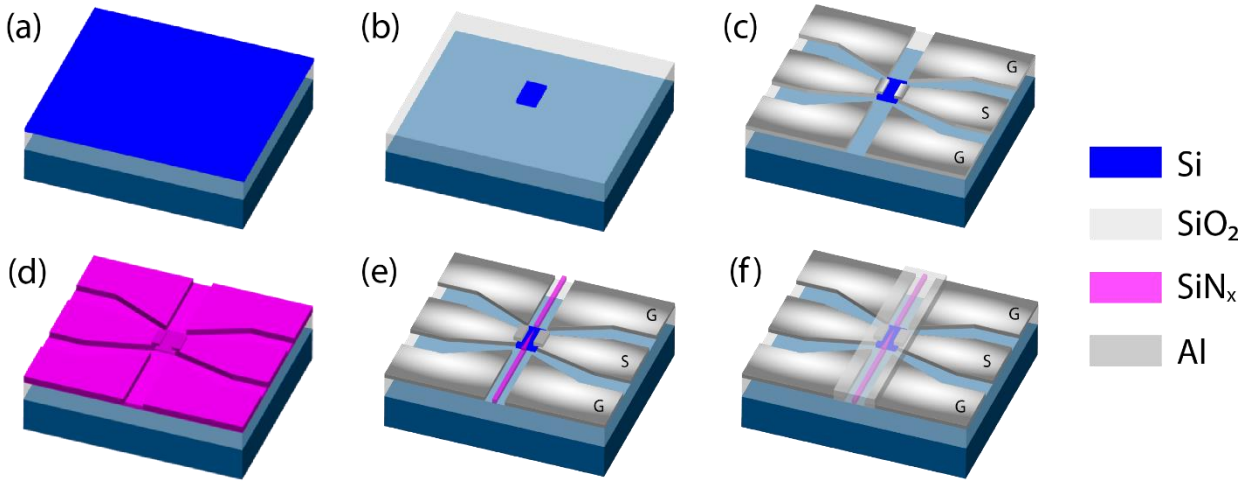

Figure 4-4 Schematic of the fabrication process (a) 250nm SOI wafer, (b) E-beam resist pattern and Si dry etch, (c) Al transmission line deposition, (d) SiN_x deposition, (e) E-beam resist pattern and SiN_x waveguide dry etch, (f) SiO_2 deposition and metal contact opening.

4.4. Results

4.4.1. Measurement

To optically control the switched, a CW 808nm fiber coupled semiconductor laser (Thorlabs FPL808S) was used. The laser is coupled into a single mode fiber where its end was cleaved and positioned to edge couple to the SiN_x input waveguide. The microwave on/off response is measured by a 2-port vector network analyzer (VNA, Agilent E8361C PNA Microwave Network Analyzer) at the frequency band from 80MHz to 40GHz. GSG probes are connected to the Al co-planar transmission lines on both ends separated by the Si photoconductive patch. S-parameter coefficients are then recorded under different optical power.

4.4.2. Performance of MORIMSs

The On/Off performances of the MORIMS are characterized by measurements of the S-parameters. The experimental details are described in the Characterization section. Figure 4-5(a) and (b) show the measured S_{21} parameter of tapered- and through-type structures at On and Off state up to ~40GHz. To characterize the switches performance, the extinction ratio $R_{on/off}=|S_{21}(On)/S_{21}(Off)|$ is adopted as the figure of merit that qualifies amplitude switching efficiency for a given microwave frequency[45]. Figure 4-5(c) and (d) show $R_{on/off}$ with respect of input optical power at frequencies of 5GHz, 20GHz and 40GHz. Overall, the On/Off ratios increase linearly from 0 to ~1.5mW before reaching a saturation plateau. As expected, the tapered-type switch shows higher performance, with switching efficiency of ~25dB and ~23dB at 5GHz and 20GHz, respectively compared to ~14dB and ~12 dB achieved at same frequencies with the through-type configuration. Although the through-type is less efficient under same incident optical power, the remaining energy in the waveguide can be used to control another switch as shown next. It is worth mentioning that the switching time of the proposed device is on the order of few micro-seconds which is compatible with beam steering and beamforming applications requirements.

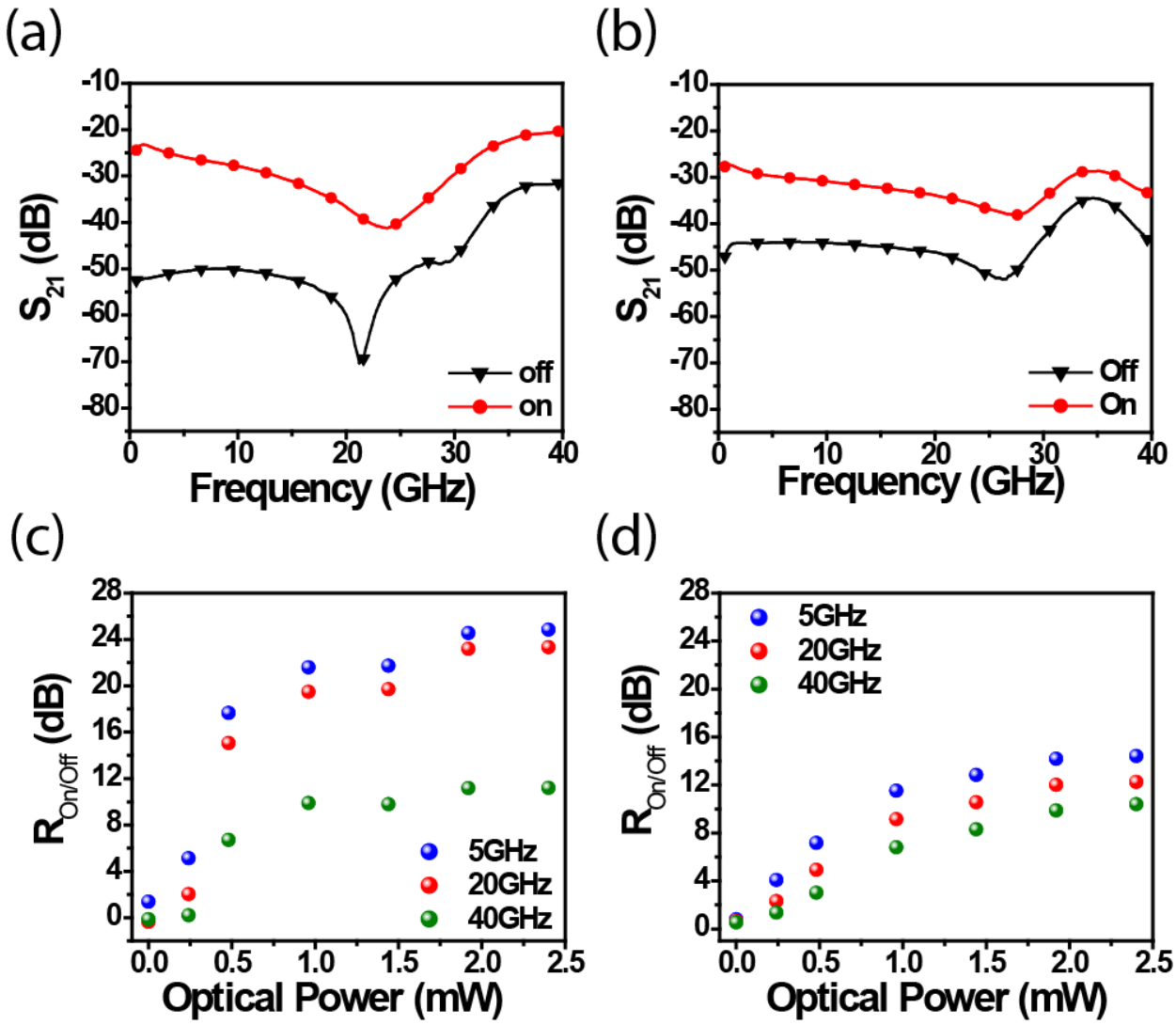

Figure 4-5 Measured S_{21} of MORIMS of (a) tapered type (b) through type; $R_{on/off}$ with respect to incident optical power of (c) tapered type (d) through type.

Table 4-1 shows the state-of-art photoconductive switches in terms of switching performances, optical power requirement and footprint. Since most of the literature has reported switching at low frequencies and few demonstrations have been done at very high frequencies, the amplitude switching performances are thus compared at frequencies below and above 10GHz. Remarkably, MORIMSs provide higher performances, i.e., ~29dB ~25dB, ~ 23dB and 11dB switching efficiency at 1, 5, 20 and 40GHz respectively, while using less than 2mW which is by

orders of magnitude lower than free-space illumination-based switches. (The optical power consumed by the Si photoconductive patch is estimated in supplementary information section III). Moreover, MORIMS shows the capability of on-chip integration which can be incorporated into complex on-chip photonics and microwave system with ultra-compact footprint to meet the desired high- packing density.

Table 4-1 Different microwave photoconductive switches with their reported frequency, S-parameter on/off ratio, power consumption and device footprint.

Year [Ref]	**$R_{on/off}$ (dB) (f≤10GHz)**	**$R_{on/off}$ (dB) (f>10GHz)**	**Optical Power requirement (mW)**	**Footprint**	**Photoconductive material**	**On-chip integration**
1995[103]	45 (1.7GHz)		143	10 μm×1.6cm	GaAs	No
2003[104]		15.4 (20GHz) 8.7 (35GHz)	90	Gap: 130 μm	GaAs	No
2003[105]	25 (1GHz)		15	1.2mm×1.4mm × 0.6mm	GaAs	No
2006[96]	15 (2GHz)		200	1mm×2mm× 0.3mm	Si	No
2006[106]		2.9 (40GHz)	100	Not report	GaAs	No
2009[48]	27.4 (2GHz)		40	$0.25cm^2$×0.5cm	Si	No
2010[44]	9 (1.5GHz)		80	100μm×5μm	GaNAsSb	No
2012[51]	18 (3GHz)		200	1mm×2mm× 0.28mm	Si	No
2012[45]			100	0.1μm×0.1μm× 150μm	GaAs	No
2015[97]	9 (3.5GHz)		20	3mm×2mm× 0.28mm	Si	No
2016[107]	5 (10GHz)		62	~1 μm×1 μm	Black Phosphorous	No
This work	**29 (1GHz) 25 (5GHz)**	**23 (20GHz) 11 (40GHz)**	**2**	**12μm×16μm× 250nm**	**Si**	**Yes**

4.4.3. Additional photoconductivity induced by the laser in Si patch calculation

To further prove that the power consumption is small for MORIMSs, we therefore estimated the additional conductivity of Si photoconductive patch at on state through the following equation[108]:

$$\Delta\sigma_s = q(\mu_n+\mu_p)a\beta\alpha\tau I_p \tag{10}$$

Where

$$I_p = \frac{P\lambda}{Ahc} \tag{11}$$

$\Delta\sigma_s$ is the additional conductivity under illumination, μ_n and μ_p are the mobility of electron and hole respectively, a is the term represents the amount of light sending into the Si photoconductive patch. β is the quantum efficiency. α is the absorption coefficient of Si at 800nm. τ is the carrier life time considering the surface recombination due to the small dimension of the Si patch. I_p is the photon density, P is the optical power, λ is the wavelength, A is the illumination area, h is the Plank constant and c is the speed of light.

The additional conductivity of the Si patch is estimated to be on the order of 2000 S/m when the incident power is at 2mW. Because our light absorbed Si region is only 16μm by 12μm, compare to the free space illumination scheme[51], the compact device design has much lesser optical power consumption.

We then calculate the S_{21}(on) at DC using the additional conductivity from Eqs. (12)-(13) through the following equation[106]:

$$S_{21}(\text{on}) = \frac{2Z_0 Gg}{1 + 2Z_0 Gg} \tag{12}$$

$$Gg = \Delta\sigma \frac{A}{L} \tag{13}$$

Where Z_0 is 50Ω, Gg is the conductance, A is the cross-section and L is the length of the Si photoconductive patch. The calculation shows S_{21} (on) is around -20dB when the additional conductivity is 2000S/m which is consistent to our experimental results at the incident power of 2mW. The S_{21} (On) of the device could be further improved by using doped wafer without sacrificing the $R_{on/off}$.

4.4.4. Performances of cascaded MORIMSs

To demonstrate scalability and integration of multiple reconfigurable switches on the same chip, three MORIMSs were designed and fabricated as depicted in Figure 4-6 (a). The MORIMSs in series and parallel configuration are fed by one single input optical waveguide. The injected light is routed toward two different paths using a 3-dB Y-branch coupler. One of the paths addresses two cascaded through-type MORIMSs. Figure 4-6 (b) – (d) show $R_{on/off}$ at different locations. Because MORIMS_1 and 3 are in parallel, they show same performance, for instance, their switching efficiency reaches ~10dB at 20GHz. However, the switching efficiency of MORIMS_2 in series with MORIMS_1, drops by only ~ 4 dB at 20GHz. To further demonstrate that this architecture has a strong potential for phased array systems, the phase shift introduced by the MORIMSs were measured. The relative phase shift of MORIMS_1 to 3 are shown in Figure 4-7. Phase shifts of 20° and 60° is achieved at 20 and 40GHz respectively. The phase change reaches saturation at relatively low optical power of about ~0.5mW. MORIMS shows promising

performances for cascaded optically reconfigurable switches for frequency and phased array system.

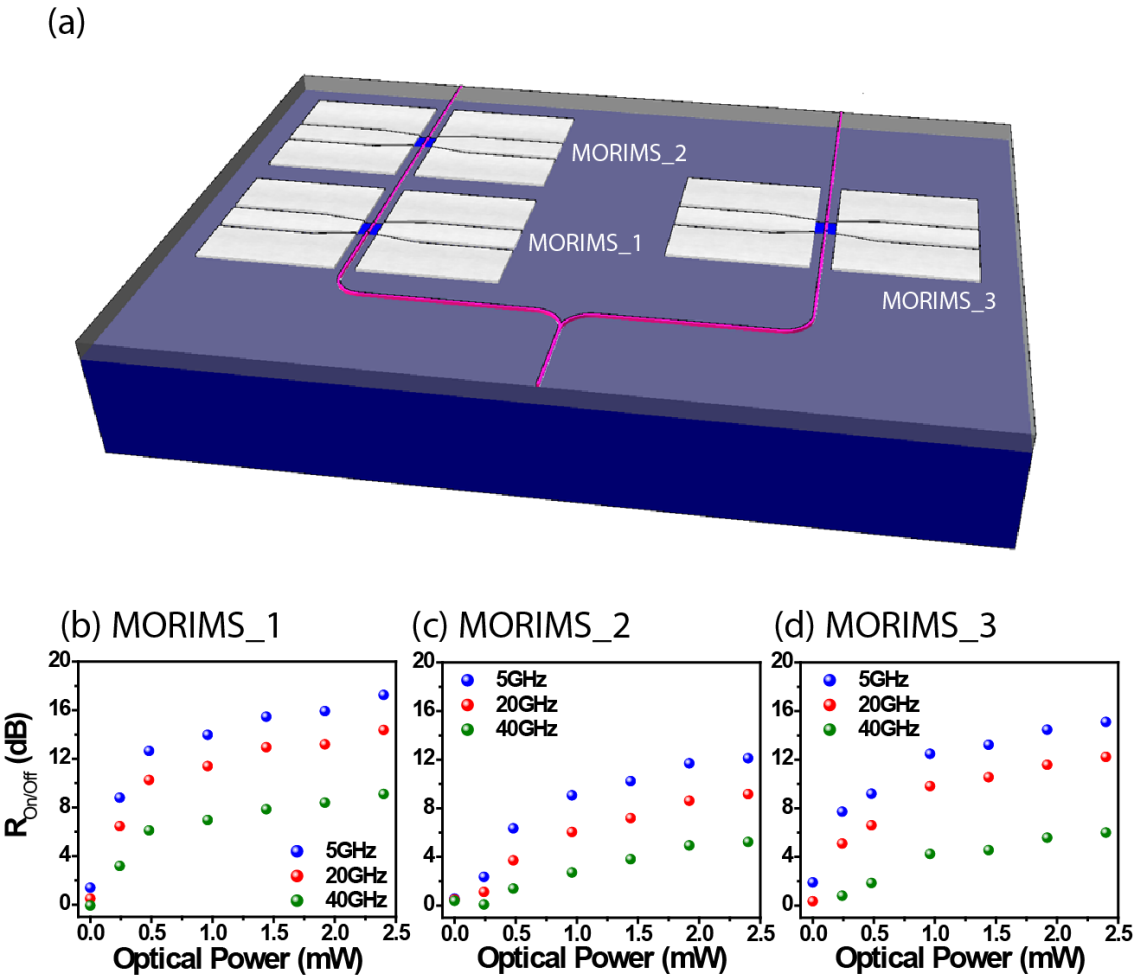

Figure 4-6 . (a) Schematic of a basic MORIMS circuit. The Ron/off at 5, 20 and 40GHz with respect to incident optical poweer of (b) MORIMS_1, (c) MORIMS_2 and (b) MORIMS_3.

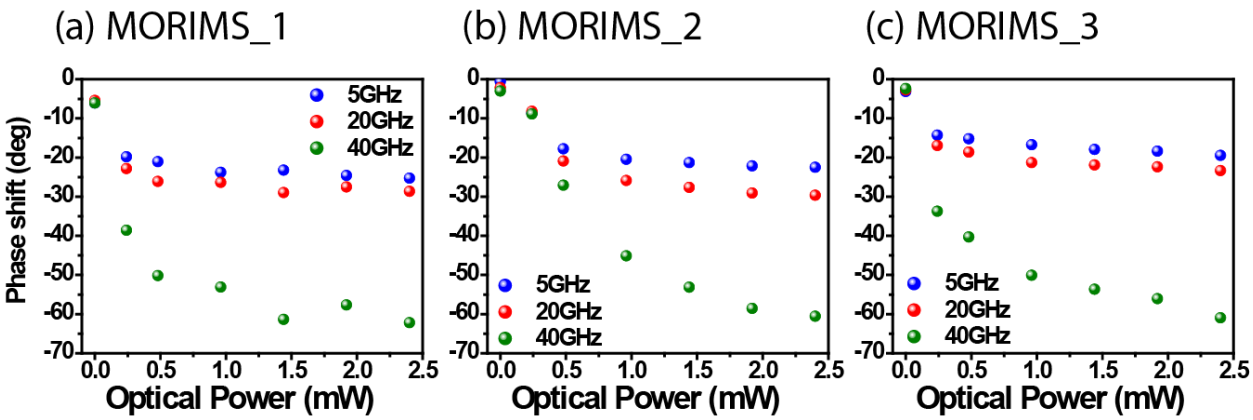

Figure 4-7 The relative phase shift at 5, 20 and 40GHz with respect to optical poweer of (a) MORIMS_1, (b) MORIMS_2 and (c) MORIMS_3. The relative positions are the same as in Fig. 3a.

4.5. Discussion and summary

The proposed optically reconfigurable switches are a proof of concept that can be easily implemented in beamforming and beam steering microwave systems which require moderate switching time constant. Moreover, the proposed integrated devices could also enable more advance functionalities when combining other well-established photonic building blocks such as ring resonators, directional couplers and Mach-Zehnder modulators on the same chip. The proposed approach can be tailored in the future generation of ultra-high frequency communications systems which will face stringent requirements in terms of frequency bandwidth, power consumption, size and packing density, and low-cost for mass production. In that area, ultra-fast photoconductive switches exploiting III-V materials, with ultra-short carrier lifetime, are required and outstanding efforts has been already made [43, p. 55], [44]. The proposed approach could be exploited in sampling application that requires the combination of several switches with very accurate time delays between them. This work is a real added value for developing integration technology for microwave signal processing.

In summary, we have demonstrated monolithic optically reconfigurable integrated microwave switches on a SOI chip. Our approach consists of co-integration of microwave circuits with integrated photonic devices to form optically reconfigurable microwave switches. A single input SiN_x waveguide is used to route the light toward switches at different location on chip. Integrated photonics provides miniaturized Si photoconductive patches, high confinement of light in the waveguide and high coupling efficiency of light from waveguide to silicon photoconductive microwave switches. Consequently, the demonstrated engineered devices outperform their classical analogues in term of On/Off switching efficiency, footprint and optical power level requirement. We experimentally demonstrate high microwave amplitude switching performances of over 25dB around 5GHz, 23dB around 20GHz and 11dB at 40GHz, and lower optical power requirement (~ 2mW) by orders of magnitude lower than the state-of-art photoconductive switches. Scalability is a challenge that has been also advanced by demonstrating integrated multiple reconfigurable switches on the same SOI chip with high amplitude switching performance. Moreover, phase shifts of 20° and 60° were measured for microwave signals at 20GHz and 40GHz, respectively. This work is an important step in introducing photonics into direct processing of microwave signals, paving the way towards optically reconfigurable microwave and millimeter wave devices for future ground, embedded radar systems, and emerging 5G wireless communication networks.

Chapter 4, in part, is a reprint of the material as it appears "Microwave signal switching on a silicon photonic chip." Fang, Cheng-Yi, Hung-Hsi Lin, Mehdi Alouini, Yeshaiahu Fainman and Abdelkrim El Amili. *(in submission)* The dissertation author was the primary coinvestigator and coauthor of this paper.

Chapter 5. Conclusion

This dissertation summarizes the work on two important components for integrated optics. The light source, nanolasers and photoconductive switches. We theoretically investigate the effect of inserting a tunnel junction in an electrically nanolaser and experimentally demonstrate the lasing action of the nanolaser. We also experimentally present on-chip photoconductive switches that is C-MOS compatible and can be a building block of integrated optics in the future.

5.1. Theoretically investigation on the tunnel junction effect on electrically pumped nanolasers

Although electrically pumped nanolasers have been an area of immense interest over the last decade, their extreme compactness still make it difficult to operate or modulate. One of the reasons is their large resistance. The large resistance results in large Joule heating when injecting current which impedes their ability to lase at room temperature. Therefore, to realize better thermal management, reducing the device resistance is essential.

We propose to insert tunnel junctions into nanolasers to reduce the device resistance and Joule heating. We conducted optical and electrical calculations combined with the results from laser rate equations to predict how tunnel junctions improve the thermal management. We also discuss how the position of tunnel junctions in nanolasers affects the optimal performance in terms of Joule heating and gain threshold. Our calculation shows the threshold voltage and Joule heating can be significantly reduced because of the reduced device resistance.

Heating is detrimental to nanolasers because heat dissipation from such small devices is extremely difficult. Therefore, inserting tunnel junctions into nanolasers is promising because heat

generation can be reduced at first place. Less heating combined with proper heat dissipation design, realizing stable room temperature electrically pumped nanolasers will be much easier.

In addition, tunnel junctions can be applied to other devices through which device heating could be significantly reduced and quantum efficiency increased. This is a giant step toward achieving extremely compact and efficient devices.

5.2. Experimental demonstration of tunnel junction incorporated electrically pumped nanolasers

We have experimentally demonstrated tunnel junction incorporated electrically pumped nanolaser. We present a new epilayer that current is injected through n-InGaAsP on both sides. The resistance is reduced by over 50% and the threshold voltage is reduced from 5V to 1V compared to nanolaser without tunnel junctions. The Joule's heating is alleviated and less input electrical power is required. We also conduct second-order coherence function measurement to prove the lasing behavior of CW electrical pumping. Moreover, we also show the metallo-dielectric nanolaser can function at 180k under CW pumping. This work paves the way for future application of tunnel junctions on other nanoscale optoelectronic devices. Less Joule heat generated can enable more stable and longer lifetime application with less input energy consumption.

5.3. Microwave signal switching on a silicon photonic chip

We propose the first monolithic optically reconfigurable microwave switches integrated in CMOS compatible silicon photonic chip. Our approach uses direct manipulation of microwave signals using microwave devices that are optically controlled. Specifically, we demonstrate monolithic integration of microwave circuits with integrated photonic control devices to form optically reconfigurable microwave switches.

The significance of this work is two folds. First, we demonstrated that the monolithic integration provides micrometer-scale switches with superior performances than the state-of-the-art devices in terms of switching efficiency, optical power level requirement, scalability and complex integration. This work constitutes a breakthrough as it addresses for the first time simultaneously all of the aforementioned stringent requirements. Secondly, this work proposes a novel generation of complex optically reconfigurable microwave circuits that benefit from the well-established integrated photonics technology. We therefore strongly believe that this work will open a new research direction in optically reconfigurable microwave circuitry on silicon photonic platforms.

Appendix A. Carrier transportation simulation

The current injection behavior was simulated in Silvaco. For the carrier transportation in the semiconductor materials. Several models were used to calculate the carrier density inside each layer.

A1. Shockley-Read-Hall (SRH) Recombination

Shockley-Read-Hall (SRH) Recombination also called trap-assisted recombination is photon transitions in the presence of a trap or defect within the forbidden gap of the semiconductor discovered by Shockley and Read [109] and then by Hall [110]. It is expressed as follow

$$R_{SRH} = \frac{pn - n_{ie}^2}{\tau_p \left[n + n_{ie} \exp\left(\frac{E_{trap}}{kT}\right)\right] + \tau_n \left[p + n_{ie} \exp\left(\frac{-E_{trap}}{kT}\right)\right]}$$

Where E_{TRAP} is the difference between the trap energy level and the intrinsic Fermi level, T is the lattice temperature in degrees Kelvin and τ_p and τ_n are the hole and electron lifetimes.

A2. Optical Generation/Radiative Recombination

Optical Generation/Radiative Recombination occurs primarily in one step and is therefore a direct generation/recombination mechanism. For band-to-band radiative recombination, an electron loses energy and drops from the conduction band to valence band. For optical generation, an electron moves from valence to conduction band. The process is modeled as follow[111]:

$$R_0 = G_0 = B_r n_0 p_0 = B_r n_i^2$$

Br is the rate of radiative capture probability. In steady-state, the rate of band-to-band radiative recombination is expressed as:

$$r = B_r np$$

$$n = n_0 + \Delta n$$

$$p = p_0 + \Delta p$$

Therefore, the net recombination rate is given by:

$$U_r = r - G_0 = B_r(np - n_i^2)$$

A3. Auger Recombination

Auger recombination is the three-particle process which involves either electron–electron collisions in the conduction band followed by recombination with holes in the valence band, or hole–hole collisions in the valence band followed by recombination with electrons in the conduction band[111]. It is modeled using the expression: [112]

$$R_{auger} = C_n(pn^2 - nn_i^2) + C_p(np^2 - pn_i^2)$$

C_n and C_p are the capture probability coefficients when the third carrier is either an electron or a hole.

BIBLIOGRAPHY

[1] M. Glick, L. C. Kimmerling, and R. C. Pfahl, “A Roadmap for Integrated Photonics,” *Optics & Photonics News, OPN*, vol. 29, no. 3, pp. 36–41, Mar. 2018.

[2] L. Thylén and L. Wosinski, “Integrated photonics in the 21st century,” *Photon. Res., PRJ*, vol. 2, no. 2, pp. 75–81, Apr. 2014.

[3] D. A. B. Miller, “Rationale and challenges for optical interconnects to electronic chips,” *Proceedings of the IEEE*, vol. 88, no. 6, pp. 728–749, Jun. 2000.

[4] D. A. B. Miller, “Optical interconnects to electronic chips,” *Appl. Opt., AO*, vol. 49, no. 25, pp. F59–F70, Sep. 2010.

[5] T. H. Maiman, “Stimulated Optical Radiation in Ruby,” *Nature*, vol. 187, no. 4736, pp. 493–494, Aug. 1960.

[6] R. N. Hall, G. E. Fenner, J. D. Kingsley, T. J. Soltys, and R. O. Carlson, “Coherent Light Emission From GaAs Junctions,” *Phys. Rev. Lett.*, vol. 9, no. 9, pp. 366–368, Nov. 1962.

[7] H. Soda, K. Iga, C. Kitahara, and Y. Suematsu, “GaInAsP/InP Surface Emitting Injection Lasers,” *Jpn. J. Appl. Phys.*, vol. 18, no. 12, p. 2329, Dec. 1979.

[8] M. T. Hill *et al.*, “Lasing in metallic-coated nanocavities,” *Nature Photonics*, vol. 1, no. 10, p. nphoton.2007.171, Sep. 2007.

[9] Q. Gu *et al.*, “Subwavelength semiconductor lasers for dense chip-scale integration,” *Adv. Opt. Photon., AOP*, vol. 6, no. 1, pp. 1–56, Mar. 2014.

[10] M. S. Lebby *et al.*, “Use of VCSEL arrays for parallel optical interconnects,” presented at the Fabrication, Testing, and Reliability of Semiconductor Lasers, 1996, vol. 2683, pp. 81–92.

[11] S. Nojima, “Single-Mode Laser Oscillation in Semiconductor Gain Photonic Crystals,” *Jpn. J. Appl. Phys.*, vol. 38, no. 8A, p. L867, Aug. 1999.

[12] O. Painter *et al.*, “Two-Dimensional Photonic Band-Gap Defect Mode Laser,” *Science*, vol. 284, no. 5421, pp. 1819–1821, Jun. 1999.

[13] R. F. Oulton *et al.*, “Plasmon lasers at deep subwavelength scale,” *Nature*, vol. 461, no. 7264, pp. 629–632, Oct. 2009.

[14] Y.-J. Lu *et al.*, “Plasmonic Nanolaser Using Epitaxially Grown Silver Film,” *Science*, vol. 337, no. 6093, pp. 450–453, Jul. 2012.

[15] Q. Zhang *et al.*, “A room temperature low-threshold ultraviolet plasmonic nanolaser,” *Nature Communications*, vol. 5, p. ncomms5953, Sep. 2014.

[16] D. J. Bergman and M. I. Stockman, “Surface Plasmon Amplification by Stimulated Emission of Radiation: Quantum Generation of Coherent Surface Plasmons in Nanosystems,” *Phys. Rev. Lett.*, vol. 90, no. 2, p. 027402, Jan. 2003.

[17] M. H. Huang *et al.*, “Room-Temperature Ultraviolet Nanowire Nanolasers,” *Science*, vol. 292, no. 5523, pp. 1897–1899, Jun. 2001.

[18] J. C. Johnson, H.-J. Choi, K. P. Knutsen, R. D. Schaller, P. Yang, and R. J. Saykally, “Single gallium nitride nanowire lasers,” *Nat Mater*, vol. 1, no. 2, pp. 106–110, Oct. 2002.

[19] S. Gradečak, F. Qian, Y. Li, H.-G. Park, and C. M. Lieber, “GaN nanowire lasers with low lasing thresholds,” *Appl. Phys. Lett.*, vol. 87, no. 17, p. 173111, Oct. 2005.

[20] R. Agarwal, C. J. Barrelet, and C. M. Lieber, “Lasing in Single Cadmium Sulfide Nanowire Optical Cavities,” *Nano Lett.*, vol. 5, no. 5, pp. 917–920, May 2005.

[21] A. Pan *et al.*, “Fabrication and Red-Color Lasing of Individual Highly Uniform Single-Crystal CdSe Nanobelts,” *J. Phys. Chem. C*, vol. 111, no. 38, pp. 14253–14256, Sep. 2007.

[22] A. Pan *et al.*, “Continuous Alloy-Composition Spatial Grading and Superbroad Wavelength-Tunable Nanowire Lasers on a Single Chip,” *Nano Lett.*, vol. 9, no. 2, pp. 784–788, Feb. 2009.

[23] D. Saxena *et al.*, “Optically pumped room-temperature GaAs nanowire lasers,” *Nature Photonics*, vol. 7, no. 12, p. nphoton.2013.303, Nov. 2013.

[24] R. Chen *et al.*, “Nanolasers grown on silicon,” *Nature Photonics*, vol. 5, no. 3, p. nphoton.2010.315, Feb. 2011.

[25] B. Mayer *et al.*, “Lasing from individual GaAs-AlGaAs core-shell nanowires up to room temperature,” *Nature Communications*, vol. 4, p. ncomms3931, Dec. 2013.

[26] J. A. Zapien *et al.*, “Room-temperature single nanoribbon lasers,” *Appl. Phys. Lett.*, vol. 84, no. 7, pp. 1189–1191, Feb. 2004.

[27] A. H. Chin, S. Vaddiraju, A. V. Maslov, C. Z. Ning, M. K. Sunkara, and M. Meyyappan, “Near-infrared semiconductor subwavelength-wire lasers,” *Appl. Phys. Lett.*, vol. 88, no. 16, p. 163115, Apr. 2006.

[28] Q. Gao *et al.*, “Selective-Area Epitaxy of Pure Wurtzite InP Nanowires: High Quantum Efficiency and Room-Temperature Lasing,” *Nano Letters*, vol. 14, no. 9, pp. 5206–5211, Sep. 2014.

[29] A. Mizrahi, V. Lomakin, B. A. Slutsky, M. P. Nezhad, L. Feng, and Y. Fainman, “Low threshold gain metal coated laser nanoresonators,” *Opt. Lett., OL*, vol. 33, no. 11, pp. 1261–1263, Jun. 2008.

[30] M. P. Nezhad *et al.*, “Room-temperature subwavelength metallo-dielectric lasers,” *Nature Photonics*, vol. 4, no. 6, p. nphoton.2010.88, Apr. 2010.

[31] J. H. Lee *et al.*, “Electrically pumped sub-wavelength metallo-dielectric pedestal pillar lasers,” *Optics Express*, vol. 19, no. 22, p. 21524, Oct. 2011.

[32] H.-G. Park *et al.*, “Electrically Driven Single-Cell Photonic Crystal Laser,” *Science*, vol. 305, no. 5689, pp. 1444–1447, Sep. 2004.

[33] K. Ding and C. Z. Ning, “Metallic subwavelength-cavity semiconductor nanolasers,” *Light Sci Appl*, vol. 1, no. 7, p. e20, Jul. 2012.

[34] M.-K. Kim, Z. Li, K. Huang, R. Going, M. C. Wu, and H. Choo, “Engineering of metal-clad optical nanocavity to optimize coupling with integrated waveguides,” *Opt. Express, OE*, vol. 21, no. 22, pp. 25796–25804, Nov. 2013.

[35] M. A. Noginov *et al.*, “Demonstration of a spaser-based nanolaser,” *Nature*, vol. 460, no. 7259, pp. 1110–1112, Aug. 2009.

[36] F. Vallini, Q. Gu, M. Kats, Y. Fainman, and N. C. Frateschi, “Carrier saturation in multiple quantum well metallo-dielectric semiconductor nanolaser: Is bulk material a better choice for gain media?,” *Optics Express*, vol. 21, no. 22, p. 25985, Nov. 2013.

[37] Q. Gu *et al.*, “Amorphous Al2O3 Shield for Thermal Management in Electrically Pumped Metallo-Dielectric Nanolasers,” *IEEE Journal of Quantum Electronics*, vol. 50, no. 7, pp. 499–509, Jul. 2014.

[38] K. Ding, M. T. Hill, Z. C. Liu, L. J. Yin, P. J. van Veldhoven, and C. Z. Ning, “Record performance of electrical injection sub-wavelength metallic-cavity semiconductor lasers at room temperature,” *Opt. Express, OE*, vol. 21, no. 4, pp. 4728–4733, Feb. 2013.

[39] E. Majda-Zdancewicz, M. Suproniuk, M. Pawłowski, and M. Wierzbowski, “Current state of photoconductive semiconductor switch engineering,” *Opto-Electronics Review*, vol. 26, no. 2, pp. 92–102, May 2018.

[40] D. H. Auston, “Picosecond optoelectronic switching and gating in silicon,” *Appl. Phys. Lett.*, vol. 26, no. 3, pp. 101–103, Feb. 1975.

[41] J. S. Sullivan and J. R. Stanley, “Wide Bandgap Extrinsic Photoconductive Switches,” *IEEE Transactions on Plasma Science*, vol. 36, no. 5, pp. 2528–2532, Oct. 2008.

[42] O. S. F. Zucker, P. K. L. Yu, and Y. Sheu, “GaN Switches in Pulsed Power: A Comparative Study,” *IEEE Transactions on Plasma Science*, vol. 42, no. 5, pp. 1295–1303, May 2014.

[43] F. Ospald *et al.*, “1.55μm ultrafast photoconductive switches based on ErAs:InGaAs,” *Appl. Phys. Lett.*, vol. 92, no. 13, p. 131117, Mar. 2008.

[44] K. H. Tan *et al.*, "1.55-mu m GaNAsSb-Based Photoconductive Switch for Microwave Switching," *IEEE Photonics Technology Letters*, vol. 22, no. 15, pp. 1105–1107, Aug. 2010.

[45] C. Tripon-Canseliet *et al.*, "Microwave On/Off Ratio Enhancement of GaAs Photoconductive Switches at Nanometer Scale," *Journal of Lightwave Technology*, vol. 30, no. 23, pp. 3576–3579, Dec. 2012.

[46] W. Shi, X. Liao, Z. Liu, and D. Ma, "Investigation of semi-insulating GaAs photoconductive switches triggered by semiconductor lasers," in *Semiconductor Lasers and Applications III*, 2008, vol. 6824, p. 682419.

[47] I. G. C. Weppelman, R. J. Moerland, J. P. Hoogenboom, and P. Kruit, "Concept and design of a beam blanker with integrated photoconductive switch for ultrafast electron microscopy," *Ultramicroscopy*, vol. 184, pp. 8–17, Jan. 2018.

[48] J. R. Flemish, H. W. Kwan, R. L. Haupt, and M. Lanagan, "A new silicon-based photoconductive microwave switch," *Microwave and Optical Technology Letters*, vol. 51, no. 1, pp. 248–252.

[49] K. B. Ali, C. R. Neve, A. Gharsallah, and J. P. Raskin, "Photo-Induced Coplanar Waveguide RF Switch and Optical Crosstalk on High-Resistivity Silicon Trap-Rich Passivated Substrate," *IEEE Transactions on Electron Devices*, vol. 60, no. 10, pp. 3478–3484, Oct. 2013.

[50] C. Tripon-Canseliet *et al.*, "High dynamic range single channel sampling of wideband RF signals using ultra-fast nanoscale photoconductive switching," *Electronics Letters*, vol. 52, no. 3, pp. 237–239, 2016.

[51] L. Lan, D. Zhao, F. Liang, Q. Zhang, and B.-Z. Wang, "Influence of laser wavelength on insertion loss of silicon-based optically controlled microwave switch," *Microwave and Optical Technology Letters*, vol. 55, no. 1, pp. 187–190.

[52] M. Ortsiefer, R. Shau, G. Böhm, F. Köhler, G. Abstreiter, and M.-C. Amann, "Low-resistance InGa(Al)As Tunnel Junctions for Long Wavelength Vertical-cavity Surface-emitting Lasers," *Japanese Journal of Applied Physics*, vol. 39, no. Part 1, No. 4A, pp. 1727–1729, Apr. 2000.

[53] S. Sekiguchi, T. Kimura, T. Miyamoto, F. Koyama, and K. Iga, "Long Wavelength GaInAsP/InP Laser with n-n Contacts Using AlAs/InP Hole Injecting Tunnel Junction," *Japanese Journal of Applied Physics*, vol. 38, no. Part 2, No. 4B, pp. L443–L445, Apr. 1999.

[54] B. P. Yonkee *et al.*, "Demonstration of a III-nitride edge-emitting laser diode utilizing a GaN tunnel junction contact," *Optics Express*, vol. 24, no. 7, p. 7816, Apr. 2016.

[55] E. Kapon and A. Sirbu, "Long-wavelength VCSELs: Power-efficient answer," *Nat Photon*, vol. 3, no. 1, pp. 27–29, Jan. 2009.

[56] Y. Zhang *et al.*, "Design and demonstration of ultra-wide bandgap AlGaN tunnel junctions," *Applied Physics Letters*, vol. 109, no. 12, p. 121102, Sep. 2016.

[57] M. X. Feng *et al.*, "High efficient GaN-based laser diodes with tunnel junction," *Applied Physics Letters*, vol. 103, no. 4, p. 043508, Jul. 2013.

[58] J. Van Campenhout *et al.*, "A Compact SOI-Integrated Multiwavelength Laser Source Based on Cascaded InP Microdisks," *IEEE Photonics Technology Letters*, vol. 20, no. 16, pp. 1345–1347, Aug. 2008.

[59] J. Van Campenhout *et al.*, "Electrically pumped InP-based microdisk lasers integrated with a nanophotonic silicon-on-insulator waveguide circuit," *Optics Express*, vol. 15, no. 11, p. 6744, 2007.

[60] J. Shane, Q. Gu, A. Potterton, and Y. Fainman, "Effect of Undercut Etch on Performance and Fabrication Robustness of Metal-Clad Semiconductor Nanolasers," *IEEE Journal of Quantum Electronics*, vol. 51, no. 1, pp. 1–9, Jan. 2015.

[61] "Theory of Optical Processes in SemiconductorsBulk and Microstructures - Oxford Scholarship," 23-Jan-2003. [Online]. Available: http://www.oxfordscholarship.com/view/10.1093/acprof:oso/9780198526209.001.0001/acprof-9780198526209. [Accessed: 03-Nov-2016].

[62] M. Sotoodeh, A. H. Khalid, and A. A. Rezazadeh, "Empirical low-field mobility model for III–V compounds applicable in device simulation codes," *Journal of Applied Physics*, vol. 87, no. 6, pp. 2890–2900, Mar. 2000.

[63] "Wiley: Physics of Photonic Devices, 2nd Edition - Shun Lien Chuang." [Online]. Available: http://www.wiley.com/WileyCDA/WileyTitle/productCd-0470293195.html. [Accessed: 04-Nov-2016].

[64] J. S. T. Smalley, Q. Gu, and Y. Fainman, "Temperature Dependence of the Spontaneous Emission Factor in Subwavelength Semiconductor Lasers," *IEEE Journal of Quantum Electronics*, vol. 50, no. 3, pp. 175–185, Mar. 2014.

[65] R.-M. Ma and R. F. Oulton, "Applications of nanolasers," *Nature Nanotechnology*, vol. 14, no. 1, pp. 12–22, Jan. 2019.

[66] D. A. B. Miller, "Are optical transistors the logical next step?," *Nature Photonics*, vol. 4, pp. 3–5, Jan. 2010.

[67] V. Dolores-Calzadilla *et al.*, "Waveguide-coupled nanopillar metal-cavity light-emitting diodes on silicon," *Nature Communications*, vol. 8, p. 14323, Feb. 2017.

[68] S. Wang *et al.*, "Unusual scaling laws for plasmonic nanolasers beyond the diffraction limit," *Nature Communications*, vol. 8, no. 1, p. 1889, Dec. 2017.

[69] D. Takahashi, S. Hachuda, T. Watanabe, Y. Nishijima, and T. Baba, “Detection of endotoxin using a photonic crystal nanolaser,” *Applied Physics Letters*, vol. 106, no. 13, p. 131112, Mar. 2015.

[70] G. Shambat *et al.*, “Single-Cell Photonic Nanocavity Probes,” *Nano Letters*, vol. 13, no. 11, pp. 4999–5005, Nov. 2013.

[71] R.-M. Ma, S. Ota, Y. Li, S. Yang, and X. Zhang, “Explosives detection in a lasing plasmon nanocavity,” *Nature Nanotechnology*, vol. 9, no. 8, pp. 600–604, Aug. 2014.

[72] Y. Nakayama *et al.*, “Tunable nanowire nonlinear optical probe,” *Nature*, vol. 447, no. 7148, pp. 1098–1101, Jun. 2007.

[73] J. Y. Suh *et al.*, “Plasmonic Bowtie Nanolaser Arrays,” *Nano Lett.*, vol. 12, no. 11, pp. 5769–5774, Nov. 2012.

[74] M. Khajavikhan *et al.*, “Thresholdless nanoscale coaxial lasers,” *Nature*, vol. 482, no. 7384, pp. 204–207, Feb. 2012.

[75] M. T. Hill *et al.*, “Lasing in metal-insulator-metal sub-wavelength plasmonic waveguides,” *Optics Express*, vol. 17, no. 13, p. 11107, Jun. 2009.

[76] K. Ding *et al.*, “Room-temperature continuous wave lasing in deep-subwavelength metallic cavities under electrical injection,” *Phys. Rev. B*, vol. 85, no. 4, p. 041301, Jan. 2012.

[77] B. P. L. SG8 9AZ. (01763) 222 333 The Sty, 47 Upper King Street, Royston, Hertfordshire, “Platinum Metals in Ohmic Contacts to III-V Semiconductors,” *Johnson Matthey Technology Review*. [Online]. Available: https://www.technology.matthey.com/article/43/1/2-12/. [Accessed: 17-Jan-2019].

[78] C. Y. Fang, F. Vallini, A. E. Amili, J. S. T. Smalley, and Y. Fainman, “Low Resistance Tunnel Junctions for Efficient Electrically Pumped Nanolasers,” *IEEE Journal of Selected Topics in Quantum Electronics*, vol. 23, no. 6, pp. 1–6, Nov. 2017.

[79] S. H. Pan, Q. Gu, A. E. Amili, F. Vallini, and Y. Fainman, “Dynamic hysteresis in a coherent high-β nanolaser,” *Optica, OPTICA*, vol. 3, no. 11, pp. 1260–1265, Nov. 2016.

[80] R. Loudon, *The Quantum Theory of Light*. OUP Oxford, 2000.

[81] J. Capmany and D. Novak, “Microwave photonics combines two worlds,” *Nature Photonics*, vol. 1, no. 6, pp. 319–330, Jun. 2007.

[82] D. Marpaung, C. Roeloffzen, R. Heideman, A. Leinse, S. Sales, and J. Capmany, “Integrated microwave photonics,” *Laser & Photonics Reviews*, vol. 7, no. 4, pp. 506–538, Jul. 2013.

[83] A. J. Seeds and K. J. Williams, “Microwave Photonics,” *Journal of Lightwave Technology*, vol. 24, no. 12, pp. 4628–4641, Dec. 2006.

[84] J. Yao, "Microwave Photonics," *Journal of Lightwave Technology*, vol. 27, no. 3, pp. 314–335, Feb. 2009.

[85] W. Liu *et al.*, "A fully reconfigurable photonic integrated signal processor," *Nature Photonics*, vol. 10, no. 3, pp. 190–195, Mar. 2016.

[86] R. Waterhouse and D. Novack, "Realizing 5G: Microwave Photonics for 5G Mobile Wireless Systems," *IEEE Microwave Magazine*, vol. 16, no. 8, pp. 84–92, Sep. 2015.

[87] I. F. da Costa *et al.*, "Optically controlled reconfigurable antenna for 5G future broadband cellular communication networks," *Journal of Microwaves, Optoelectronics and Electromagnetic Applications*, vol. 16, no. 1, pp. 208–217, Mar. 2017.

[88] A. Karabegovic, R. M. O'Connell, and W. C. Nunnally, "Photoconductive switch design for microwave applications," *IEEE Transactions on Dielectrics and Electrical Insulation*, vol. 16, no. 4, pp. 1011–1019, Aug. 2009.

[89] X. Yi, T. X. H. Huang, and R. A. Minasian, "Photonic Beamforming Based on Programmable Phase Shifters With Amplitude and Phase Control," *IEEE Photonics Technology Letters*, vol. 23, no. 18, pp. 1286–1288, Sep. 2011.

[90] A. Andy, P. Alizadeh, K. Z. Rajab, T. Kreouzis, and R. Donnan, "An optically-switched frequency reconfigurable antenna for cognitive radio applications," in *2016 10th European Conference on Antennas and Propagation (EuCAP)*, 2016, pp. 1–4.

[91] H.-J. Song *et al.*, "Microwave Photonic Mixer Utilizing an InGaAs Photoconductor for Radio over Fiber Applications," *IEICE TRANSACTIONS on Electronics*, vol. E90-C, no. 2, pp. 457–464, Feb. 2007.

[92] M. Burla, L. Romero Cortés, M. Li, X. Wang, L. Chrostowski, and J. Azaña, "On-chip programmable ultra-wideband microwave photonic phase shifter and true time delay unit," *Optics Letters*, vol. 39, no. 21, p. 6181, Nov. 2014.

[93] C. Wang, P. Fang, J. Guo, T. Lin, and C. Lee, "Sub-Second Switching Speed Polarization-Independent 2 pi Terahertz Phase Shifter," *IEEE Photonics Journal*, vol. 9, no. 6, pp. 1–7, Dec. 2017.

[94] K. S. Kelkar, N. E. Islam, C. M. Fessler, and W. C. Nunnally, "Silicon carbide photoconductive switch for high-power, linear-mode operations through sub-band-gap triggering," *Journal of Applied Physics*, vol. 98, no. 9, p. 093102, Nov. 2005.

[95] W. Shi, C. Ma, and M. Li, "Research on the Failure Mechanism of High-Power GaAs PCSS," *IEEE Transactions on Power Electronics*, vol. 30, no. 5, pp. 2427–2434, May 2015.

[96] C. J. Panagamuwa, A. Chauraya, and J. C. Vardaxoglou, "Frequency and beam reconfigurable antenna using photoconducting switches," *IEEE Transactions on Antennas and Propagation*, vol. 54, no. 2, pp. 449–454, Feb. 2006.

[97] D. Zhao, Y. Han, Q. Zhang, and B.-Z. Wang, “Experimental study of silicon-based microwave switches optically driven by LEDs,” *Microwave and Optical Technology Letters*, vol. 57, no. 12, pp. 2768–2774.

[98] D. Patron, K. R. Dandekar, and A. S. Daryoush, “Optical control of pattern-reconfigurable planar antennas,” in *2013 IEEE International Topical Meeting on Microwave Photonics (MWP)*, 2013, pp. 33–36.

[99] Y. Yashchyshyn, S. Malyshev, A. Chizh, P. Bajurko, and J. Modelski, “Study of active integrated photonic antenna,” in *2009 3rd European Conference on Antennas and Propagation*, 2009, pp. 3507–3510.

[100] M. Asghari and A. V. Krishnamoorthy, “Silicon photonics: Energy-efficient communication,” *Nature Photonics*, 01-May-2011. [Online]. Available: https://www.nature.com/articles/nphoton.2011.68. [Accessed: 15-Oct-2018].

[101] D. Pérez *et al.*, “Multipurpose silicon photonics signal processor core,” *Nature Communications*, vol. 8, no. 1, Dec. 2017.

[102] M. Smit, J. van der Tol, and M. Hill, “Moore’s law in photonics,” *Laser & Photonics Reviews*, vol. 6, no. 1, pp. 1–13, Jan. 2012.

[103] S. E. Saddow and C. H. Lee, “Optical control of microwave-integrated circuits using high-speed GaAs and Si photoconductive switches,” *IEEE Transactions on Microwave Theory and Techniques*, vol. 43, no. 9, pp. 2414–2420, Sep. 1995.

[104] C. Canseliet, C. Algani, F. Deshours, G. Alquie, S. Formont, and J. Chazelas, “A novel optically-controlled microwave switch on semiconductor substrates for an ON/OFF ratio enhancement,” in *33rd European Microwave Conference Proceedings (IEEE Cat. No.03EX723C)*, 2003, vol. 1, pp. 265-268 Vol.1.

[105] Y. Kaneko *et al.*, “Microwave switch: LAMPS (light-activated microwave photoconductive switch),” *Electronics Letters*, vol. 39, no. 12, pp. 917–919, Jun. 2003.

[106] C. Tripon-Canseliet *et al.*, “Optically controlled microwave phase shifting and sampling by efficient photoconductive switching on LT-GaAs substrate integrated technology,” in *Photonics North 2006*, 2006, vol. 6343, p. 63432K.

[107] “Exploring the promising properties of 2D exfoliated black phosphorus for optoelectronic applications under 1.55 μm optical excitation | (2016) | Penillard | Publications | Spie.” [Online]. Available: http://spie.org/Publications/Proceedings/Paper/10.1117/12.2223585. [Accessed: 23-Oct-2018].

[108] W. Platte, “Effective photoconductivity and plasma depth in optically quasi-CW controlled microwave switching devices,” *IEE Proceedings J - Optoelectronics*, vol. 135, no. 3, pp. 251–254, Jun. 1988.

[109] W. Shockley and W. T. Read, “Statistics of the Recombinations of Holes and Electrons,” *Phys. Rev.*, vol. 87, no. 5, pp. 835–842, Sep. 1952.

[110] R. N. Hall, “Electron-Hole Recombination in Germanium,” *Phys. Rev.*, vol. 87, no. 2, pp. 387–387, Jul. 1952.

[111] S. S. Li, “Excess Carrier Phenomenon in Semiconductors,” in *Semiconductor Physical Electronics*, S. S. Li, Ed. New York, NY: Springer New York, 2006, pp. 134–170.

[112] J. Dziewior and W. Schmid, “Auger coefficients for highly doped and highly excited silicon,” *Appl. Phys. Lett.*, vol. 31, no. 5, pp. 346–348, Sep. 1977.